Do Loop Current Eddies stimulate productivity in the Gulf of Mexico?

Pierre Damien[(1,2)], Julio Sheinbaum[(1)], Orens Pasqueron de Fommervault[(1)], Julien Jouanno[(3)], Lorena Linacre[(4)], Olaf Duteil[(5)]

[(1)] Departamento de Oceanografía Física, Centro de Investigación Científica y de Educación Superior de, Ensenada, México,

[(2)] University of California, Los Angeles, CA

[(3)] LEGOS, Université de Toulouse, IRD, CNRS, CNES, UPS, Toulouse, France,

[(4)] Departamento de Oceanografía Biológica, Centro de Investigación Científica y de Educación Superior de Ensenada, México,

[(5)] GEOMAR Helmholtz Centre for Ocean Research, Kiel, Germany.

Corresponding author: Pierre Damien (pdamien@ucla.edu)

Key Points :

- LCEs trigger a local phytoplankton biomass increase in winter.
- Chlorophyll variability at surface does not reflect the seasonal cycle of the depth-integrated biomass.
- Convective mixing and Ekman pumping are key mechanisms to preferentially supply nutrient toward the euphotic layer in LCEs.

Abstract

Surface chlorophyll concentrations inferred from satellite images suggest a strong influence of the mesoscale activity on biogeochemical variability within the oligotrophic regions of the Gulf of Mexico (GoM). More specifically, long-living anticyclonic Loop Current Eddies (LCEs) are shed episodically from the Loop Current and propagate westward. This study addresses the biogeochemical response of the LCEs to seasonal forcing and show their role in driving phytoplankton biomass distribution in the GoM. Using an eddy resolving (1/12°) interannual regional simulation, it is shown that the LCEs foster a large biomass increase in winter in the upper ocean. It is based on the coupled physical-biogeochemical model NEMO-PISCES that yields a realistic representation of the surface chlorophyll distribution. The primary production in the LCEs is larger than the average rate in the surrounding open waters of the GoM. This behavior cannot be directly identified from surface chlorophyll distribution alone since LCEs are associated with a negative surface chlorophyll anomaly all year long. This anomalous biomass increase in the LCEs is explained by the mixed-layer response to winter convective mixing that reaches deeper and nutrient-richer waters.

I/ Introduction

Historical satellite ocean color observations of the deep waters of the Gulf of Mexico (roughly delimited by the 200m isobath and from hereafter referred to as GoM open-waters) indicate low surface chlorophyll concentrations ([CHL]), low biomass and low primary productivity (Müller-Karger et al., 1991; Biggs and Ressler, 2001; Salmerón-García et al., 2011). The GoM open-waters are mostly oligotrophic, as confirmed by more recent bio-optical in-situ measurements from autonomous floats (Green et al., 2014; Pasqueron de Fommervault et al., 2017; Damien et al., 2018). The surface chlorophyll concentration in the GoM open-waters exhibits a clear seasonal cycle which is primarily triggered by the seasonal variation of the mixed layer depth (Müller-Karger et al., 2015) and river discharges (Brokaw et al., 2019). In tandem, the seasonal cycle is strongly modulated by the energetic mesoscale dynamic activity which shapes the distribution of biogeochemical properties (Biggs and Ressler, 2001; Pasqueron de Fommervault et al., 2017). This mesoscale activity is dominated by the large and long-living Loop Currents Eddies (LCEs) which are shed episodically by the Loop Current (Weisberg and Liu, 2017) and constitute the most energetic circulation features in the GoM (Sheinbaum et al., 2016; Sturges & Leben, 2000).

Mesoscale activity (see McGuillicuddy et al., 2016 for a review) modulates the phytoplankton biomass distribution (Siegel et al., 1999; Doney et al., 2003; Gaube et al., 2014; Mahadevan, 2014) and the ecosystem functioning (McGillicuddy et al., 1998, Oschlies and Garcon, 1998, Garcon et al., 2001). Specifically, the ability of the mesoscale eddies to enhance vertical fluxes of nutrients is determinant in sustaining the observed phytoplankton growth rate in oligotrophic regions such as the GoM open-waters, where the phytoplankton primary production is limited by nutrient availability in the euphotic layer (McGillicuddy and Robinson 1997; McGillicuddy et al., 1998; Oschlies and Garcon, 1998).

54 The upward doming of isopycnals in cyclonic eddies and downward depressions in anticyclonic
55 eddies, also known as “eddy-pumping”, occur when the eddies are strengthening (Siegel et al., 1999,
56 Klein and Lapeyre, 2009) and produce a vertical nutrient transport. This has been historically proposed
57 as the dominant mechanism controlling the mesoscale biogeochemical variability, as it induces a
58 reduction of productivity in the anticyclone and an increase in cyclones. This paradigm is however
59 challenged by observations of enhanced surface chlorophyll concentrations in anticyclonic eddies
60 (Gaube et al., 2014), particularly during winter (Dufois et al., 2016). As a plausible explanation, eddy-
61 wind interactions may significantly modulate vertical fluxes through Ekman transport divergence
62 within the eddies (Martin and Richards, 2001, Gaube et al., 2013, 2015). This mechanism is
63 responsible for a downwelling in the core of cyclones and an upwelling in the core of anticyclones.
64 Dufois et al. (2014, 2016) link these observations to a deeper mixed layer in anticylonic eddies. This is
65 explained by the eddy-driven modulation of the upper ocean stratification which directly affects the
66 winter convective mixing (He et al., 2017). Observed mixed layers tend to be deeper in anticyclones
67 than in cyclones (Williams, 1998; Kouketsu et al., 2012) and vertical nutrient fluxes to the euphotic
68 layer are potentially enhanced in anticyclones during periods prone to convection (e.g. winter in the
69 GoM). Although some consensus exists on the fundamental role of anticyclonic eddies on the
70 productivity of oligotrophic ocean regions, large uncertainties remain regarding the relative importance
71 of the different mechanisms involved in the biogeochemical responses.

72 Besides, in-situ measurements in oligotrophic regions have shown that the surface [CHL]
73 variability, observed from ocean color satellite imagery, is not necessarily representative of the total
74 phytoplankton (carbon) biomass variability in the water column (Siegel et al., 2013; Mignot et al.,
75 2014). In particular, a surface [CHL] winter increase, may result from physiological mechanisms (i.e.
76 modification of the ratio of [CHL] to phytoplankton carbon biomass) or from a vertical redistribution
77 of the phytoplankton (Mayot et al., 2017) rather than from changes in the biomass content. It is not

clear yet which of these hypotheses holds in oligotrophic regions, and more specifically in the GoM open-waters where this issue has been addressed by in-situ sub-surface [CHL] observations (Pasqueron de Fommervault et al., 2017). Most of the studies focusing on chlorophyll variability use surface (or near-surface) [CHL] as a proxy for phytoplankton biomass and interpret a [CHL] increase as an effective biomass production. Only a few studies considered the vertically integrated responses (Dufois et al., 2017; Guo et al., 2017; Huang and Xu, 2018) emphasizing the importance of considering the eddy impact on the subsurface.

The objective of this study is to better understand the role of LCEs in driving [CHL] distribution and variability within the GoM open-waters. Material and methods used in this study are presented in section 2. In section 3, the imprint of the LCEs on the surface [CHL] distribution is inferred from satellite ocean color observations. Since these measurements are confined to the oceanic surface layer and do not allow access to the vertical properties of LCEs, we complete the analysis with a coupled physical-biogeochemical simulation (subsections 2 and 3). Particular attention is paid to the validation of the modeled LCE dynamical structures and surface [CHL] anomalies. In the last section, we propose to disentangle the mesoscale mechanisms controlling the seasonal cycle of the [CHL] vertical profile in LCEs. The model also enables to assess both abiotic and biotic processes and physical-biogeochemical interactions that can be difficult to address with in-situ observations only.

II/ Material and methods

II.1/ The coupled physical-biogeochemical model

97 The simulation analyzed in this study (referred as GOLFO12-PISCES) has been described and
98 compared with observations in Damien et al. (2018). It relies on a physical-biogeochemical coupled
99 model based on the ocean model NEMO (Nucleus for European Modeling of the Ocean, version 3.6;
100 Madec, 2016) and the biogeochemical model PISCES (Pelagic Interaction Scheme for Carbon and
101 Ecosystem Studies; Aumont and Bopp, 2006; Aumont et al., 2015). The model grid covers the GoM
102 and the western part of the Cayman Sea (Fig 1) with a 1/12° horizontal resolution (~ 8.4 km). This
103 allows to resolve scales related to the first baroclinic mode, which is of the order of 30-40 km in the
104 GoM open-waters (e.g., Chelton et al., 1998). The model is forced with realistic open-boundary
105 conditions from the MERCATOR reanalysis GLORYS2V3, high frequency atmospheric forcing based
106 on an ECMWF ERA-interim reanalysis (Brodeau et al., 2010), and freshwater and nutrient-rich
107 discharges from rivers (Dai and Trenberth, 2002). The open-boundary conditions of biogeochemical
108 tracers are prescribed from the World Ocean Atlas observation database (Garcia et al., 2010) for NO_3,
109 O_2, Si, and PO_4, and from the global configuration ORCA2 (Aumont & Bopp, 2006) for DIC, DOC,
110 Alkalinity, and Fe. The other state variables are forced arbitrary very small constant values. The
111 analysis has been performed using 5-day averaged outputs for a period of 5 years from 2002 to 2007.
112 We refer the reader to Damien et al. (2018) for an extended model and numerical setup descriptions. In
113 this previous study, an extensive validation of the modeled properties were carried out , focusing on
114 physical properties that are known to influence primary production and chlorophyll concentration: the
115 mixed layer depth and the depth and slope of the nutricline. A novel aspect was to use in-situ
116 observations collected from autonomous floats and published in Green et al. (2014) and Fommervault
117 et al. (2017) to validate not only the modeled surface chlorophyll concentration but also the chlorophyll
118 vertical profile in the GoM. To be able to reproduce the vertical profile of chlorophyll correctly, the
119 parameters of the biogeochemical model were largely tuned compared to the ones suitable for global
120 simulations (Aumont et al., 2015). The ability of GOLFO12-PISCES to reproduce the main observed
121 features of the GoM was demonstrated, at least at a basin and seasonal scale.

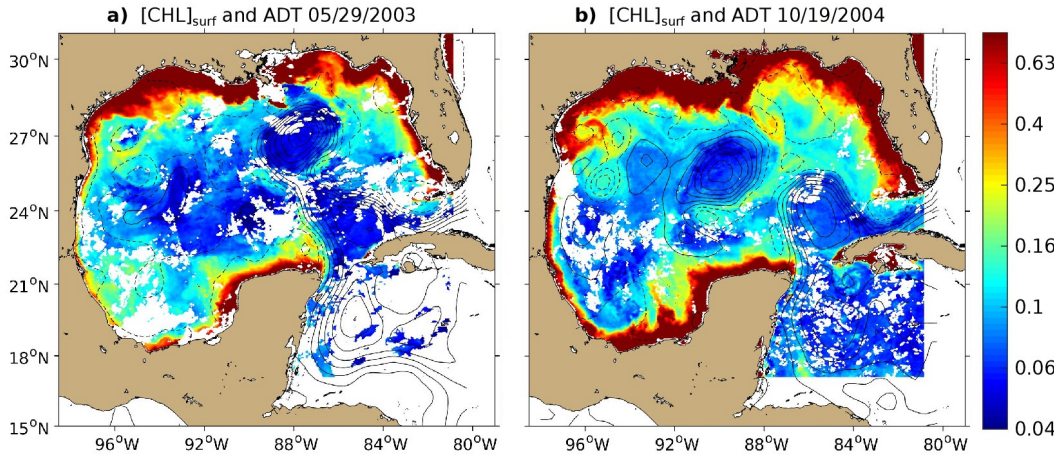

Figure 1: 8-days composite images of $[CHL]_{surf}$ (in $mg \cdot m^{-3}$) around (a) May 29th 2003 and (b) October 19th 2004 derived from Aqua-MODIS images overlaid with contours of Absolute Dynamic Topography (ADT in m) derived from Aviso images are superimposed. Contour interval is 10cm and ADT values lower than 40cm are shown with dashed curves.

II.2/ Observational Data Set Used

Satellite observations are used to evaluate the ability of GOLFO12-PISCES to reproduce the dynamical and biological signatures associated with LCEs. Surface geostrophic velocities are derived from a 1/4° multi-satellite merged product of absolute dynamic topography (ADT) provided by AVISO+ (http://marine.copernicus.eu). Surface chlorophyll concentrations are from the Aqua-MODIS 4 km product (Sathyendranath et al., 2012; http://marine.copernicus.eu) and consist of 8-day composites from 2003 to 2015.

II.3/ LCEs detection, tracking and composite construction

In order to track the LCEs, we use the algorithm developed by Nencioli et al. (2010), which has been extensively employed to track coherent mesoscale eddies (Dong et al., 2012, Ciani et al. 2017, Zhao et al. 2018) and submesoscale eddies (Damien et al., 2017). It is based on the geometric organization of the velocity fields, dominated by rotation, that develop around eddy centers. Here, it is applied to weekly AVISO+ surface geostrophic velocities and GOLFO12-PISCES 5-day averaged velocities at 20m depth. The selection of LCEs is defined using the criteria that eddies have to be shed from the Loop Current.

In order to assess the [CHL] response to LCE dynamics, eddy-centric horizontal images and transects of LCEs are used to make composites constructed by averaging modeled variables of the different LCEs collocated to their center. The transect building procedure involves an axisymmetric averaging that assumes axis-symmetry of the dynamical structures and no tilting of their rotation axis. Moreover, we choose not to consider the LCEs formation period and the LCEs destruction period when reaching the western basin (Lipphardt et al., 2008; Hamilton et al., 2018) as LCE destruction/formation involves specific processes (Frolov et al., 2004; Donohue et al., 2016). We therefore focus on the LCEs contained in the central part of the GoM from 86°W to 94°W. Annual composites are computed along with monthly composite averages in order to assess seasonal variability. Composite LCEs averaged during the months of January and February are referred to as winter composites and those averaged during July and August are referred to as summer composites. These composites provide an overview of the LCEs mean hydrographical, biogeochemical and dynamical characteristics.

II.4/ Diagnostics

The LCE radius R_{LCE} is estimated as the radial distance between the center and the peak azimuthal velocity V_{max}. The mixed layer depth (MLD), a major physical factor influencing nutrient distribution and [CHL] dynamics (Mann and Lazier, 2006), is defined as the depth at which potential density exceeds its value at 10m depth by 0.125 $kg \cdot m^{-3}$ (Levitus, 1982; Monterey and Levitus, 1997). The stratification of the water column is evaluated by the square of the buoyancy frequency

$N^2(z) = \frac{-g}{\rho_0} \frac{\partial \rho}{\partial z}$, where g is the gravitational acceleration, z is depth, ρ is density and ρ_0 is a reference density.

As carried out in Damien et al. (2018), several metrics are defined and used to describe [CHL]:

- $[CHL]_{surf}$: [CHL] averaged between 0 and 30 m depth, and considered as surface concentration (in mg $CHL \cdot m^{-3}$),
- $[CHL]_{tot}$: integrated content of [CHL] over the 0-350 m layer (in mg $CHL \cdot m^{-2}$),
- DCM: depth of the Deep Chlorophyll maximum (in m),
- $[CHL]_{DCM}$: [CHL] value at DCM depth (in mg $CHL \cdot m^{-3}$).

To understand the mesoscale distribution of [CHL], key biological variables are vertically integrated between 0 and 350m: the phytoplanktonic concentration $[PHY]_{tot}$, the primary production rate PP_{tot} and the grazing rate GRZ_{tot}. PP_{tot} consists of two components: new production PPN_{tot} fueled by nutrients supplied from a source external to the mixed layer and regenerated production PPR_{tot} sustained by recycled nutrients within the euphotic layer (Dugdale & Goering, 1967; Eppley & Peterson, 1979). The euphotic depth corresponds to 1% of the incoming photosynthetic active radiation at surface and reaches between 120 and 150 m in the GoM (Jolliff et al., 2008; Linacre et al., 2019). A chlorophyll concentration anomaly within LCEs, [CHL]', is computed as $[CHL]' = [CHL] - \overline{[CHL]}$, where $\overline{[CHL]}$ is the averaged background [CHL] field in the open GoM waters (for radius>250km from the LCEs'

centers). We also define the normalized anomaly as $[CHL]'/SD([CHL]')$ with SD the standard deviation operator, following a similar approach as Gaube et al. (2013, 2014) and Dufois et al. (2016). To limit the influence of very high [CHL] values in coastal waters under the direct influence of continental discharges, a salinity filtering criterion (lower than 36 psu) is applied. A similar method was used by Gaube et al. (2013, 2014) to filter edge effects but using a distance criterion instead.

III/ Results

III.1/ Satellite observations of [CHL]

Fig 1 shows the 8-day averaged satellite observations of the surface chlorophyll around May 29th 2003 (a) and October 19th 2004 (b). These observations highlight the strong contrast between the eutrophic conditions in the coastal waters and the oligotrophic conditions in the open ocean, as already addressed by several studies (Martinez-Lopez & Zavala-Hidalgo, 2009; Pasqueron de Fommervault et al., 2017). Far from the coast, these figures also reveal that the surface chlorophyll varies at a scale of the order of 100km with a distribution that tends to follow the absolute dynamic topography (ADT) contours.

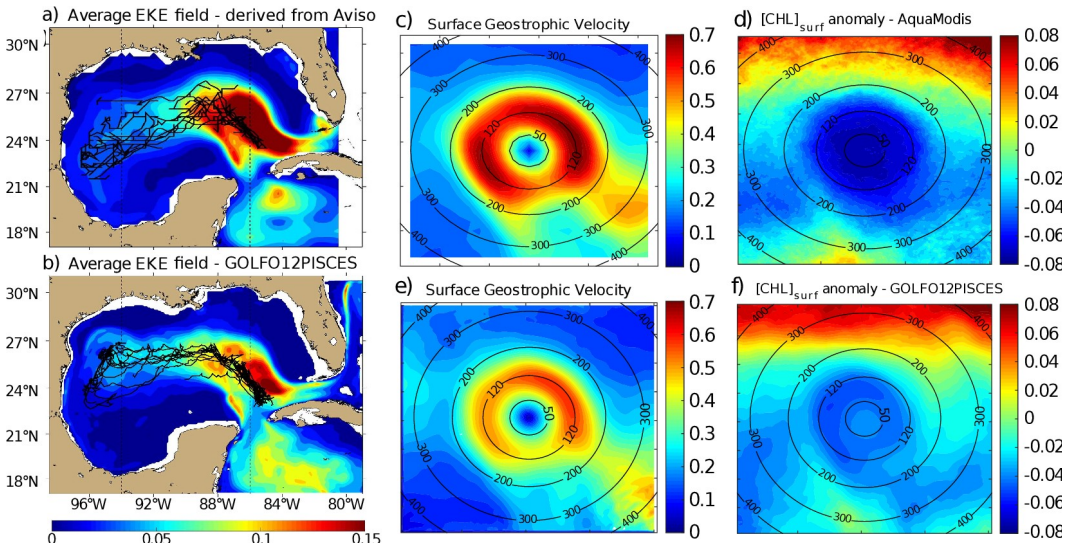

Figure 2: Average eddy kinetic energy (EKE) field derived from (a) Aviso geostrophic surface velocities and from (b) GOLFO12-PISCES currents at 10m depth. The trajectories of the tracked LCEs are superimposed to the EKE field (black lines). Vertical black dashed lines indicate the central GoM area over which composites are built. Annual LCE composite images of surface geostrophic velocities for (c) Aviso images and (e) GOLFO12-PISCES. Annual LCE composite images of surface chlorophyll concentration anomaly for (d) Modis images and (f) GOLFO12-PISCES. Black circles indicate the radius in kilometers.

LCEs trajectories are reported on Fig 2.a, superimposed onto the geostrophic climatological eddy kinetic energy (EKE) field at the surface. EKE is computed from eddy velocities defined on each grid cell as the difference between the total horizontal current and its mean value over 120 days. This time window is chosen to filter the seasonal signal. EKE is concentrated in the LC and on the westward pathway of the LCEs (Lipphardt et al. 2008) demonstrating that LCEs constitute the major source of EKE in the GoM open waters (Sheinbaum et al., 2016; Sturges & Leben, 2000; Hamilton, 2007; Jouanno et al., 2016).

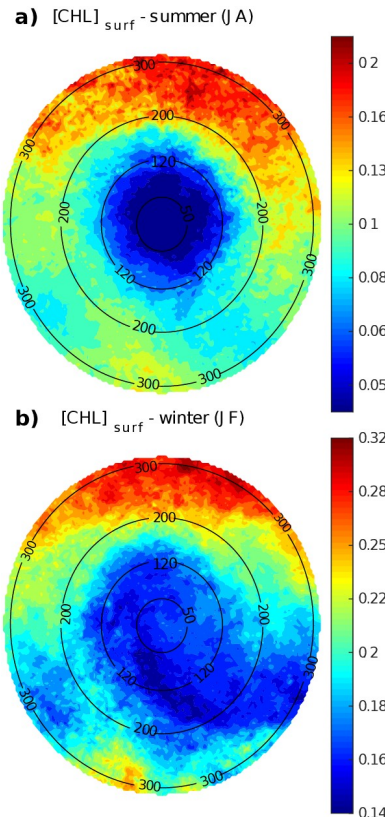

Figure 3: LCE composite images of $[CHL]_{surf}$ derived from Aqua-MODIS for the (a) summer and (b) winter seasons. Black circles indicate the radius in kilometers.

LCE annual composites of surface geostrophic velocities (Fig 2.c) and $[CHL]_{surf}$ (Fig 2.d) are built from 482 different satellite images. On average, we found that R_{LCE} ~ 120 km and V_{max} ~ 0.6-0.7 $m \cdot s^{-1}$, in agreement with previously reported LCEs (Elliot, 1982; Cooper et al., 1990; Forristal et al., 1992; Glenn and Ebbesmeyer, 1993; Weisberg and Liu, 2017; Tenreiro et al., 2018). LCEs are associated with a negative $[CHL]_{surf}$ anomaly (~ -0.07 $mg.m^{-3}$ in the annual average). The LCEs influence on $[CHL]_{surf}$ is largest in summer (Fig 3.a) when it reaches very low values (< 0.045 $mg \cdot m^{-3}$), which corresponds to an anomaly of ~ -0.08 $mg \cdot m^{-3}$. This anomaly is less remarkable in winter (~ -0.06 $mg.m^{-3}$, Fig 3.b) when $[CHL]_{surf}$ ~ 0.17 $mg \cdot m^{-3}$ within LCEs. The high chlorophyll concentrations in the northern part of the composites (in the southern part too but in smaller proportions) are related to shelves.

III.2/ Dynamical characterization of modeled LCEs

A total of 11 model LCEs were detected during the 5 years of simulation. Their trajectories are reported in Fig 2.b, superimposed upon the climatological EKE field simulated at 10 meters. The westward / southwestward propagation of LCEs is well reproduced (Vukovich, 2007) even though the LCEs translation is almost westward in GOLFO12-PISCES. Comparison with Fig 2.a shows the ability of GOLFO12-PISCES to represent the mean and transient dynamical features of the GoM open waters (also see Garcia-Jove et al., 2016).

The robustness of the composite method arises from the number of LCE used to build the composites:

- Annual composite is built from 605 5-day averaged LCEs model outputs from 10 different LCEs,
- Summer composite is built from 83 5-day averaged LCEs model outputs from 8 different LCEs,
- Winter composite is built from 93 5-day averaged LCEs model outputs from 9 different LCEs.

The model LCEs surface geostrophic velocities (Fig 2.e) have important similarities with velocities inferred from altimetry (Fig 2.c) confirming that GOLFO12-PISCES reproduces the surface signature of the LCEs. However, one can also notice an underestimation of the surface orbital velocities (~ 25% on average over the 50-200 km radius range). This bias could result from the relatively coarse model resolution and 5-day output frequency that are unable to fully capture the gradient intensity at R_{LCE}. The assumption of an axial symmetry of the LCE circulation around its center also induces an error that tends to decrease V_{max}.

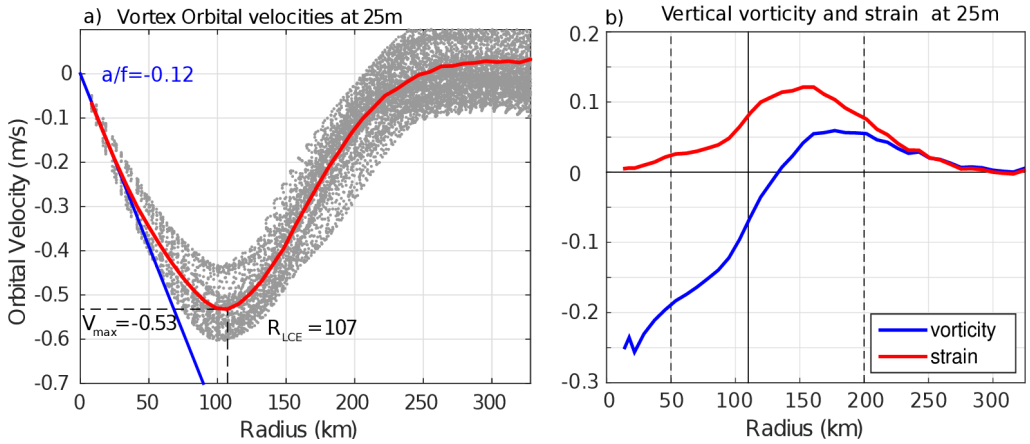

Figure 4: (a) Orbital velocities at 25m depth in function of the radius of each detected LCE (light gray dots). The red line is the LCE orbital velocity profile of the annually-averaged composite. (b) Vertical vorticity and strain computed from the averaged orbital velocity profile assuming no radial velocity in cylindrical coordinates as $\zeta_z = \frac{1}{fr}\frac{\partial rv}{\partial r}$ **and** $S = \frac{1}{f}\left(\frac{\partial v}{\partial r} - \frac{v}{r}\right)$.

Orbital velocities of composite eddies are used to distinguish different dynamical areas within LCEs. The model annual average dynamical profile at 25m depth (Fig 4) reveals a typical vortex-like structure with R_{LCE} ~ 107 km and V_{max} ~ 0.53 m·s^{-1} and suggests the following decomposition:

- r < 50 km : the **LCEs core**, where the eddy is approximately in solid body rotation: $V_{orb} = a \cdot r$ where the coefficient a is related to the Rossby number (Ro = 2a/f). The ratio a/f is estimated to be ~ -0.12 (Fig. 4). In this field, the stain is reduced to a minimum and the flow is dominated by rotation.
- 50 km < r < 200 km: the **LCEs ring** structure where the orbital velocity reaches its maximum at R_{LCE} and then decreases. The horizontal strain is important in this field, even dominating vorticity from radius exceeding R_{LCE}.
- r > 200 km: the **background GoM**, where the velocity anomalies related to the LCE vanish.

In the vertical (Fig 5.a), LCEs are near-surface intensified anticyclonic vortex rings. At depth, the orbital peak velocity decreases rapidly. At 500 m depth, V_{max} ~ 0.17 m·s^{-1} and R_{LCE} ~ 75 km, and the dynamical LCE signal nearly vanishes below 1500 m depth (V_{max} < 0.03 m·s^{-1}). The proposed division into 3 distinct dynamical regions applies from the surface down to 500 m depth (Fig 5.a).

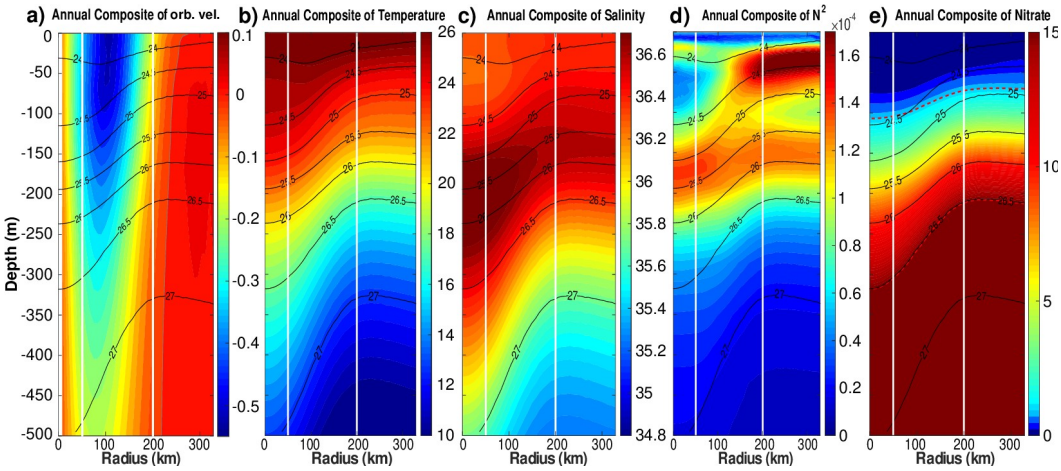

Figure 5: Annually-averaged LCE composite transects of (a) orbital velocities [m/s], (b) potential temperature [°C], (c) salinity [psu], (d) squared Brunt-Väisälä frequency (N^2 in s^{-2}) and (e) nitrate concentration [mmol·m^{-3}]. Isopycnals anomalies (black contours) are superimposed on all panels. Vertical white lines delimit the three dynamical fields of the LCE composite. On panel e, dashed red lines highlights two specific iso-nitrate contours: 1 and 15 mmol·m^{-3}.

The composite hydrological structure of modeled LCEs is shown in Fig 5.b and 5.c. The depression of isopycnals, associated with a depression of isotherms and isohalines, is characteristic of oceanic anticyclones. In the core of the eddies, the composite depicts a salinity maximum located between 100 and 300 m, corresponding to the signature of the Atlantic Subtropical UnderWater (ASTUW) of Caribbean origin entering the GoM through the Yucatan Channel (Badan et al., 2005; Hernandez-Guerra & Joyce, 2000; Wuust, 1964). This salinity maximum is not limited to the core of the LCE but gradually erodes and shallows: 36.82 psu at 200 m in the LCEs core and 36.61 psu at 150 m in the background GoM common water. Details on the fate of this salinity maximum investigated with GOLFO12 simulations can be found in Sosa-Gutiérrez et al. (2020). The ASTUW layer (salinity >

36.5 psu) is also thicker in the LCEs core (~190 m thick) compared to the background GoM water (~120 m thick). Overall, GOLFO12-PISCES reproduces the observed hydrological structure of LCEs (Elliott, 1982; LeHenaff et al., 2012; Hamilton et al., 2018; Meunier et al., 2018b).

The annually averaged LCE composite presents a lens-shaped structure exhibiting a ~50 m thick layer of weakly stratified waters located between 50 and 100 m depth (Fig 5.d). This subsurface modal water presents hydrological characteristics close to the observed background GoM waters (potential temperature ~25.4°C and salinity ~ 36.3 psu, Meunier et al., 2018b) and is surrounded below and above by well stratified layers (Meunier et al., 2018a). The upper pycnocline varies seasonally and vanishes in winter due to the deepening of the mixed layer, whereas the lower pycnocline is permanent.

The downward displacement of isopycnals is accompanied by a depletion of nutrients in the upper layer of the LCEs core (Fig 5.e). This is a typical feature of mesoscale anticyclones in the ocean (McGillicuddy et al. 1998; Oschlies and Garcon, 1998). The 1 mmol.m^{-3} iso-nitrate concentration (hereafter Z_{NO3}, sometimes referred to as the nitracline as in Cullen & Eppley, 1981; Pasqueron de Fommervault et al., 2017 or Damien et al., 2018) is located at ~ 70 m depth in the background GoM waters whereas it is found much deeper in the core (Z_{NO3} ~ 106 m). At depth, iso-nitrate layers and isopycnals are well correlated (Ascani et al., 2013; Omand & Mahadevan, 2014). For instance, iso-nitrate concentration of 15 mmol·m^{-3} follows the displacements of the 1026.5 kg·m^{-3} isopycnal. However, above 150 m, the density/nitrate relation is different inside and outside the eddies (Z_{NO3} is collocated with isopycnal 1024.4 kg·m^{-3} in the LCEs core while it is on isopycnal 1024.9 kg·m^{-3} in the background GoM).

III.3/ Surface and vertical distribution of chlorophyll in LCEs

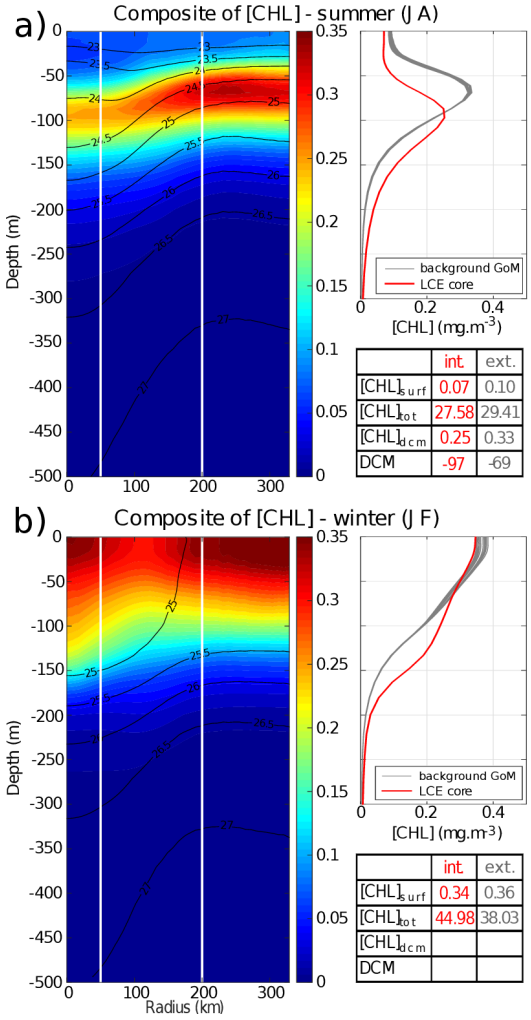

Figure 6: LCE composite transects of [CHL] during summer season (A) and winter season (B). Density anomalies (black contours) are superimposed. Vertical white lines delimit the three dynamical fields of the LCE composite. For each season, [CHL] profiles in the LCE core (r < 50 km, red lines) and in the background GoM (200 km < r < 330 km, gray lines) are plotted. Key metrics concerning [CHL] profiles are also indicated in the tables.

The large difference in stratification between the LCEs core and background GoM suggests a contrasted seasonal response of the [CHL]. This is evidenced by the analysis of summer and winter composites of [CHL] vertical distribution:

- In summer (Fig 6.a), $[CHL]_{surf}$ is ~ 30% lower in the LCEs core (r < 50km) than in the background GoM (200 km < r < 330 km). A pronounced DCM, characteristic of oligotrophic environments, is deeper in the core (~ 97 m) than in the background GoM (~ 69 m) with chlorophyll concentrations significantly lower in the interior (~ - 25%).

- In winter, the [CHL] is maximum at the surface in all the composite domains (Fig 6.b). $[CHL]_{surf}$ is lower in the LCEs core compared to the background GoM but the difference is less marked (~ - 6%) than in summer. The main discrepancy is the depth of the inflection point of these profiles. It is deeper in the LCEs core (~-150 m), resulting in a more homogenized [CHL] over a deeper layer than in the background GoM (~-120 m).

However, despite reduced surface concentration both in winter and summer, the integrated chlorophyll content, $[CHL]_{tot}$, shows a distinct seasonal pattern compared to the surface (tables in Fig 6):

- In summer, $[CHL]_{tot}$ is lower in the LCEs core (27.58 $mg \cdot m^{-2}$) compared to the background GoM (29.41 $mg \cdot m^{-2}$) and $\Delta[CHL]_{tot}$ = -1.83 $mg \cdot m^{-2}$,
- In winter, $[CHL]_{tot}$ is higher in the LCEs core (44.98 $mg \cdot m^{-2}$) compared to the background GoM (38.03 $mg \cdot m^{-2}$) and $\Delta[CHL]_{tot}$ = + 6.95 $mg \cdot m^{-2}$.

The winter increase of $[CHL]_{tot}$ is around 29% in the background GoM whereas it reaches 63% in the LCEs core, leading to $[CHL]_{tot}$ in the core being larger than $[CHL]_{tot}$ in the background GoM in winter. Meanwhile, $[CHL]_{surf}$ remains lower within the LCEs core. The fact that the [CHL] at the surface does not reflect its depth-integrated behavior means that the peculiar variability of [CHL] within LCEs may not be fully captured by ocean color satellite measurements. This is consistent with Pasqueron de Fommervault et al. (2017) and Damien et al. (2018) observations and modeling results which addressed the vertical [CHL] distribution in the GoM.

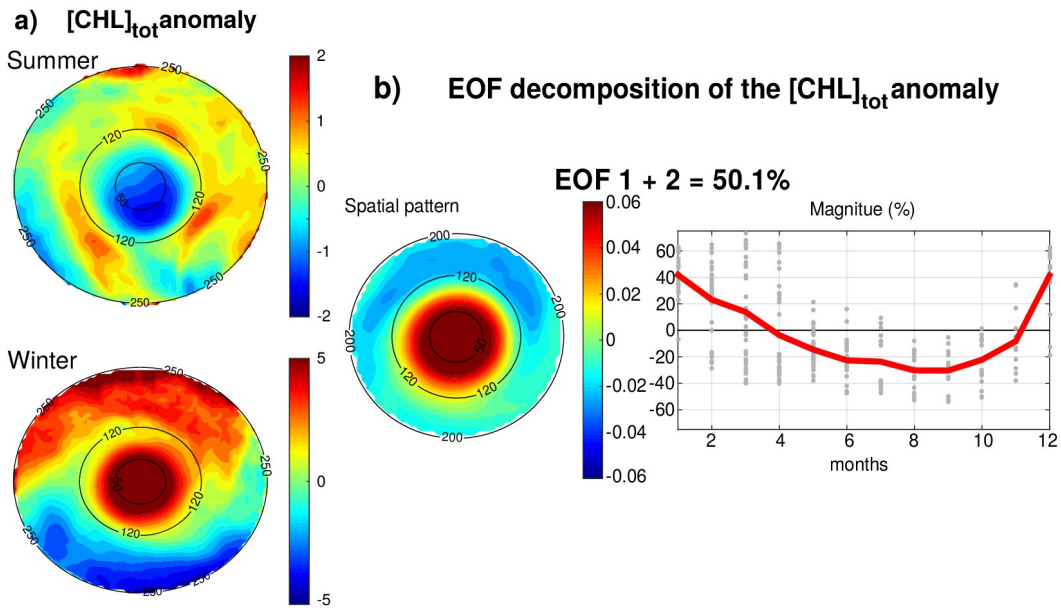

316 **Figure 7: (a) Anomaly of $[CHL]_{tot}$ in summer and winter seasons. Black circles indicate the radius in kilometers. (b) EOF**
317 **decomposition of the normalized $[CHL]_{tot}$ anomaly. The spatial patterns and monthly magnitude (gray dots; the red line**
318 **represents their monthly averaged value) of the two first modes are indicated. Modes 1 and 2 were summed together (upper**
319 **panel) and represent 50.1% of the total variance.**

320 $[CHL]_{tot}$ is strongly shaped by both the seasonal variability and the LCEs. The seasonal
321 composites of $[CHL]_{tot}$, shown in Fig 7.a, confirm the summer/winter contrast and highlight a
322 monopole structure with a relatively homogeneous distribution of $[CHL]_{tot}$ within the eddy's core. In
323 order to better characterize the spatio-temporal variability of $[CHL]_{tot}$ induced by LCEs, an Empirical
324 Orthogonal Function (EOF) analysis was performed on the normalized $[CHL]_{tot}$ anomaly (Fig 7.b)
325 following the methodology of Dufois et al. (2016). It consists in decomposing the signal into
326 orthogonal modes of variability. Here, we choose to focus on the first two most significant modes
327 which explain 40.2% and 9.9% of the variability. Since they both depict a similar monopole structure
328 in the LCEs core, they were added up in a mode referred to EOF 1+2 responsible for 50% of the total
329 $[CHL]_{tot}$ variance within LCEs. The third eigenmode (not shown) accounts for 6.2% and depicts a
330 dipole structure with opposite polarity located at the east and north of the eddy center. On average, the

EOF1+2 mode is positive in winter (from December to March) and negative the rest of the year (from April to November), with a maximum in January December and a minimum in September. This justifies, a posteriori, the choice to consider winter and summer LCE composites.

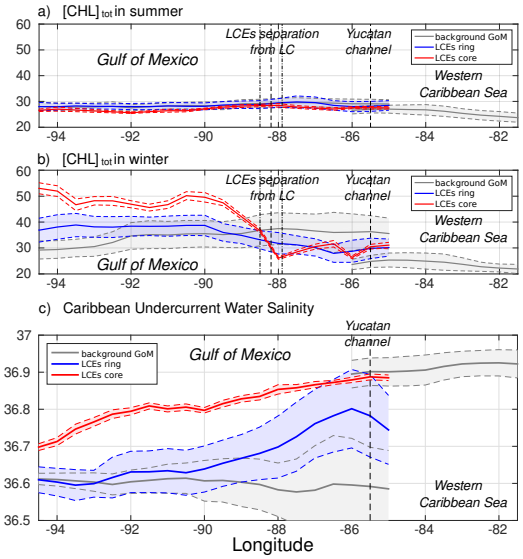

Figure 8: (a) Summer $[CHL]_{tot}$, (b) winter $[CHL]_{tot}$ and (c) salinity of Caribbean waters (ASTUW defined as the subsurface salinity maximum) as a function of longitude in (red) the LCEs core, (blue) the LCEs ring and in (gray) the background GoM. Full lines indicate the averaged value and dashed lines the +/- one standard deviation interval.

The composite evolution of the LCEs $[CHL]_{tot}$ along their westward journey is shown in Fig 8.a and 8.b. It illustrates how the total chlorophyll concentration is preferentially increased in winter within the LCEs core, as soon as the LCEs are shed from the LC. The winter $[CHL]_{tot}$ within LCEs is much larger (exceeding one standard deviation) than the background winter $[CHL]_{tot}$. In terms of integrated [CHL], the LCEs-induced seasonal variability overwhelms the GoM open-waters background seasonal variability.

IV/ Discussion

In an oligotrophic environment such as the GoM open-waters, the primary production is generally limited by nutrient supply and $[CHL]_{tot}$ exhibits low seasonal variability at the GoM basin scale (Pasqueron de Fommervault et al., 2017). The winter increase of $[CHL]_{tot}$ within the LCEs core (which translates into an effective increase of biomass, see appendix A) contrasts and may have large implications for the regional biogeochemical cycles and ecosystem structuration. It also echoes several studies which report elevated $[CHL]_{surf}$ within anticyclonic eddies in the oligotrophic subtropical gyre of the southeastern Indian Ocean (Martin and Richards, 2001; Waite et al., 2007; Gaube et al., 2013; Dufois et al., 2016, 2017; He et al., 2017), questioning the classical paradigm of low productivity usually associated with anticyclonic eddies.

The mechanisms explaining the LCE impact on [CHL] are discussed below, trying to rationalize the respective role of abotic (e.g., trapping, winter mixing, Ekman pumping) and biotic processes (e.g., primary production (PP), grazing pressure, regenerated versus new PP).

IV.1 Eddy trapping

The distinct hydrological and biogeochemical properties associated with the LCEs core suggest their ability to trap and transport oceanic properties. This mechanism, known as the eddy-trapping (Early et al., 2011; Lehahn et al., 2011; McGillicuddy, 2015; Gaube et al., 2017), is efficient only if the orbital velocities of the vortex are faster than the eddy propagation speed (Flierl, 1981; d'Ovidio et al., 2013). The rotational velocities of the model LCEs are ~ $0.53 m \cdot s^{-1}$ are one order of magnitude larger than the propagation velocities (~ $0.046 m \cdot s^{-1}$ on average). This suggests that LCEs might have a

363 certain ability to trap the water masses present in their core with relatively low exchanges with the
364 exterior.

365 Salinity is well-suited to investigate water masses trapped within the LCEs core during their
366 propagation toward the western GoM (Fig 8.c; Sosa-Gutierez et al., 2020): salinity distribution shows a
367 marked subsurface maximum that is not affected by biogeochemical processes. In the Western
368 Caribbean Sea, ASTUW is characterized by high salinity (~ 36.9 psu on average) and low standard
369 deviation (< 0.05 psu). The eastern GoM salinity field reveals that most of the ASTUW crosses the
370 Yucatan Channel within the Loop Current. During the formation of LCEs, a significant part of
371 ASTUW is captured into the LCEs core with low alteration of its properties (Fig 5.c and 8.c). Within
372 the LCEs core, the water mass is transported from eastern to the western GoM where its salinity
373 decreases from 36.9 psu to 36.7 psu. Although altered, the ASTUW signature is still clearly detectable
374 in the GoM western boundary. The other part of ASTUW entering the GoM is found in the LCEs ring.
375 Compared to the core, the salinity in the ring is on average lower (~ 36.8 psu in the eastern GoM) and
376 presents a high standard deviation, pointing out that more recent ASTUW co-exists with older ASTUW
377 that yields lower salinity maxima. As LCEs travel westward across the GoM, salinity in the LCEs ring
378 decays rapidly to reach values similar to the background GoM values (~ 36.6 psu). This
379 homogenization mainly arises from vertical mixing and winter mixed layer convection (Sosa-Gutierez
380 et al., 2020). Horizontal intrusions and filamentation may also contribute to this homogenization
381 (Meunier et al., 2020). The composites also suggest that almost no ASTUW enters the GoM apart from
382 the LCEs. The slight increase of the background salinity from eastern to western GoM is a consequence
383 of the diffusion of salt from the LCEs toward the exterior.

384 Although LCEs undergo considerable decaying rates, their erosion is particularly strong in the
385 ring while the core remains better isolated from the surrounding waters (Lehahn et al., 2011; Bracco et

al., 2017). Since no significant $[CHL]_{tot}$ seasonal variability is reported in the Western Caribbean Sea (Fig. 8), the biogeochemical behavior in the LCEs core has then to be driven by local processes with low influence of horizontal advective process from the ring or of the Caribbean waters trapped during the LCEs formation. Given that the LCEs core is also quite homogeneous, the following discussion relies on the analysis of the seasonal cycles of selected parameters averaged within the LCEs core.

IV.2 Nitracline depth and nutrient supply into the mixed layer

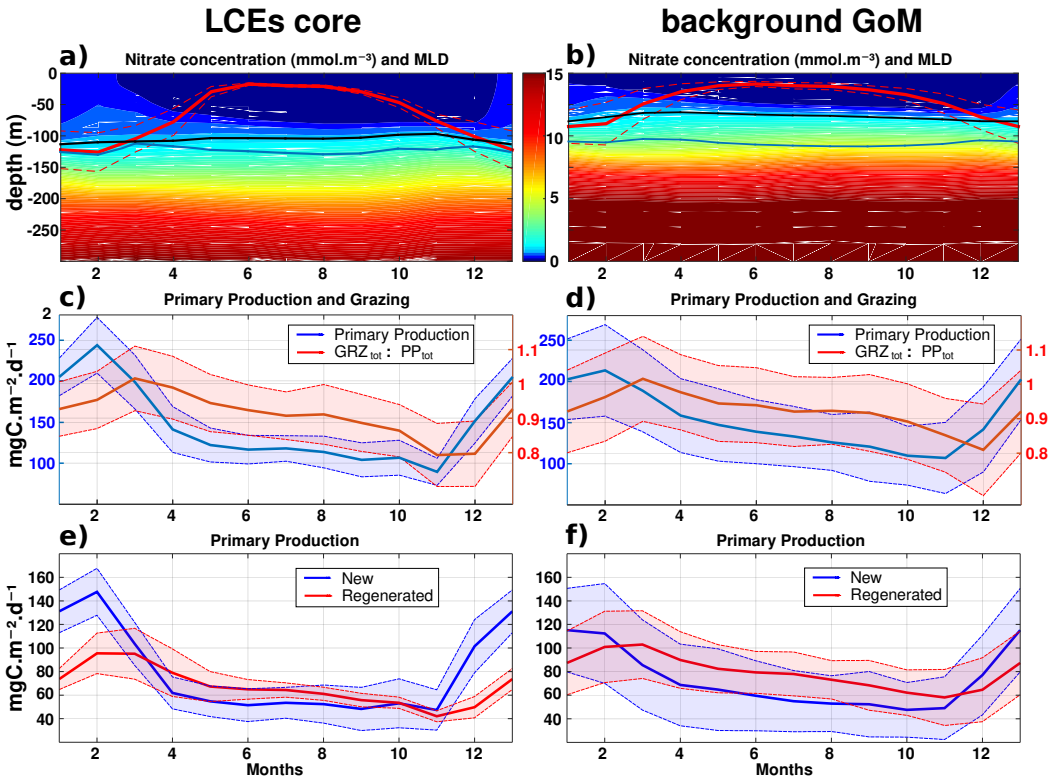

Figure 9: Climatological seasonal cycles of (a and b) nitrate concentration profiles (the red line overlaid is the average mixed layer depth, the blue line is the base of the euphotic layer and the black line the nitracline), (c and d) the total primary production (blue) and the ratio of grazing rate over primary production (red) and (e and f) the new (blue) and regenerated (red) primary production. The left panels (a, c and e) refer to the seasonal time series in the LCEs core (r < 50 km) whereas the right panels (b, d

and f) refer to the seasonal time series in the background GoM (r > 200 km). For each average cycle, the mean value is shown (full line) along with its variability (+/- 1 standard deviation relative to the mean, dashed lines).

The LCEs impact the upper ocean stratification (Fig 5.d), the nutricline depth (Fig 5.e) and consequently the nutrient supply to the euphotic layer (McGillicuddy et al., 2015). The relationship between mixed layer deepening and nutrient supply is studied here by comparing the Z_{NO3} with the MLD (Fig 9.a,b).

In late-spring and summer (from May to September), the water column is stratified (shallow MLD) and the downward displacement of the isopycnals within the LCEs pushes nutrients below the euphotic zone (see also Figs 5.e, 6.a): less nutrients are available within the LCE cores for phytoplankton growth, explaining a deeper and less intense DCM. In winter, the convective mixing, fostered both by intense buoyancy losses and strong mechanical energy input at the surface, causes a larger deepening of the mixed layer within the LCEs core (~ - 125 m, Fig 9.a) compared to the background (~ - 85 m, Fig 9.b). This asymmetry is due to a pronounced decrease of the surface and subsurface stratification within the LCE core (Fig 5.d, Kouketsu et al., 2012). A quantitative diagnostic of the stratification is given by the columnar buoyancy, $\int_0^H N^2(z).z.\mathrm{dz}$ which measures the buoyancy loss required to mix the water column to a depth H (Herrmann et al. 2008). Fig 10.a reveals significant differences in pre-winter buoyancy between the eddy core and its surroundings. Assuming that the change in buoyancy content is mainly controlled by the buoyancy flux at the surface (see Turner 1973; Lascaratos & Nittis, 1998), it suggests that mixing the water column down to ~ -210 m depth requires smaller surface buoyancy loss in LCEs cores compared to the background GoM (Fig 10.b).

However, the larger winter deepening of the mixed layer within the LCEs core is not a sufficient condition to explain a larger nutrient supply. Indeed, it fosters the transport of nutrients from the nitracline toward the mixed layer because both are getting closer. Fig 10.c highlights that a smaller buoyancy loss mixes down the water column to greater nutrient concentration levels in the LCEs core compared to the LCEs surrounding. This likely explains the winter increase of surface nitrate concentration within the LCEs (Fig 9.a). In addition, a diagnostic of the different contributions to [NO_3] evolution is proposed in appendix B. It shows the dominant role of vertical advection and diffusion in winter in providing nutrients to the euphotic layer in the LCEs core.

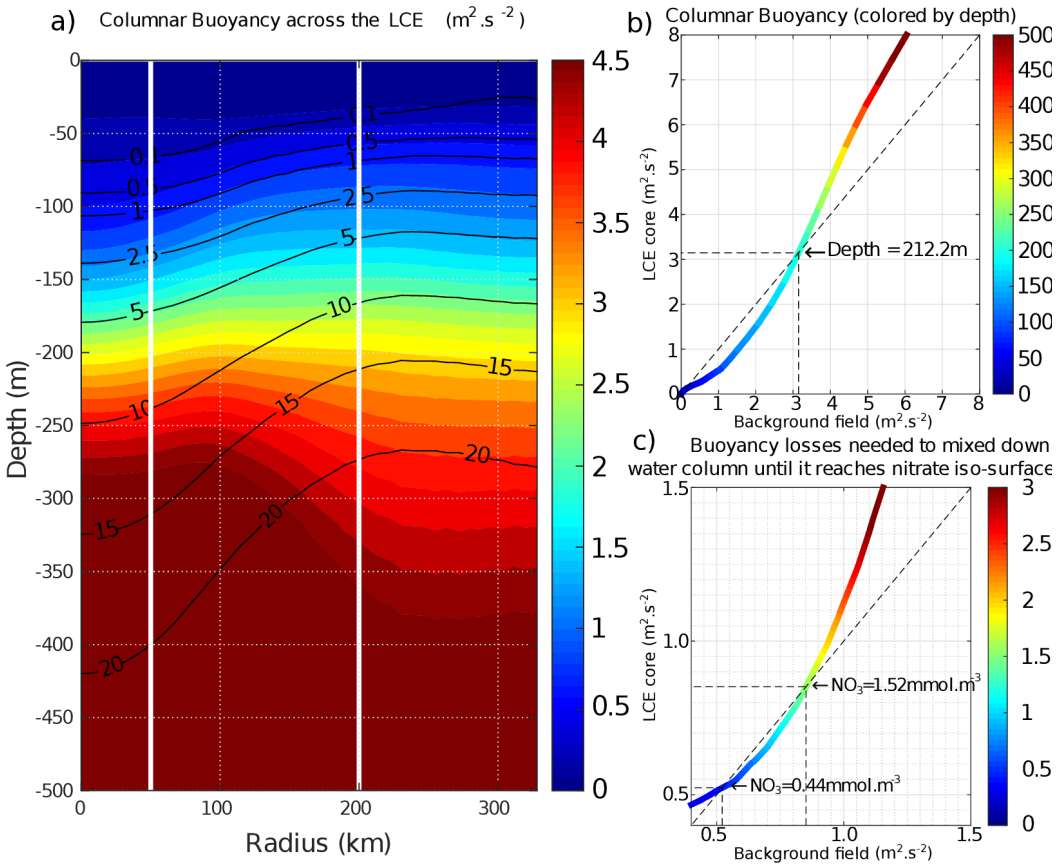

Figure 10: (a) Columnar Buoyancy transect composite in summer, corresponding to pre-winter mixing season. Iso-nitrate concentrations (black contours) are superimposed. Vertical white lines delimit the three dynamical fields of the LCE composite. (b) Vertical increase of the columnar buoyancy in the LCEs core versus the background GoM. Colors refer to depth. (c) Columnar buoyancy loss required to mix the water column down to the iso-nitrate surface defined by the line color.

So far we have assumed that the surface buoyancy fluxes are identical over the LCEs core and the background GoM. However, this is not strictly the case because temperature/salinity features in the LCEs and background waters are different (Fig 5.b,c; see also Williams 1988). The modeled surface buoyancy loss during winter season is ~18 % more intense within the LCEs. This difference is substantial and probably mainly driven by additional surface cooling applied on the warm LCE core through air-sea interaction. It contributes to enhance convection within the eddies core, and then nutrient supply toward the surface.

IV.3 Productivity and grazing

The primary productivity PP_{tot} presents a clear seasonal cycle both in the LCEs cores and in the background GoM with lower values in October-November, a sharp increase starting in November, a maximum in February and a gradual decrease from March to October (Fig 9.c.d). The annual PP_{tot} is slightly lower in the LCEs core (~ 142.4 $mgC \cdot m^{-2}.d^{-1}$) than in the background GoM (~ 148.9 $mgC \cdot m^{-2}.d^{-1}$). The amplitude of the seasonal cycle is larger in the LCEs core: from April to November, PP_{tot} is on average ~12% lower in the LCEs core whereas, in winter, PP_{tot} is ~14% higher where it reaches ~ 243.2 $mgC \cdot m^{-2}.d^{-1}$ in February. Particularly in the LCE core, the PP_{tot} seasonal cycle is tightly correlated with vertical mixing revealing the important role of mixing in the biogeochemistry. The relatively low standard deviation of the monthly PP_{tot} distribution in the LCE core also supports the idea that the influence of the seasonal variability of the forcing largely overwhelms their interannual and sub-monthly variability (Fig 9.c).

The ratio of the PPN_{tot} and PPR_{tot} provides information about the mechanisms controlling the biomass growth (Fig 9.e and 9.f). In winter, the PPN_{tot} plays a leading role, reaching up to 113-147 $mgC \cdot m^{-2} \cdot d^{-1}$, driven by the winter mixing and induced NO_3 fluxes (see Appendix B). Conversely, the PPR_{tot} is dominant from April to October. During this period, low NO_3 resources are available in the euphotic layer and the ecosystem preferentially uses ammonium to sustain the PP_{tot}. This seasonal pattern is characteristic of oligotrophic environments such as the GoM open waters (Wawrik et al., 2004; Linacre et al., 2015). In winter, changes in PP_{tot} are correlated to the intensity of winter mixing in the LCEs core (Fig 9.c) and the background GoM (Fig 9.d). The larger PPN_{tot} in the eddy core is consistent with a larger supply of NO_3 and evidences that the core of anticyclones can be preferential spots of enhanced biological production.

The pressure exerted by zooplankton grazers varies seasonally (Fig 9.c .d). It shows a similar seasonal cycle in the LCEs core and in the background GoM. On average, ~ 90% of the total growth is consumed by grazers, reaching the highest impact in March, just one month after the peak season of the PP_{tot} in both areas. In February the difference between the primary production and the grazing rate tends to be larger in the LCEs core (GRZ_{tot}/PP_{tot} = 0.95 +/- 0.08) than in the GoM background (GRZ_{tot}/PP_{tot} = 0.96 +/- 0.13, Fig. 9.c), leading to an enhanced net primary production. Considering the ecosystem from a “top-down” perspective, the grazing rate also participates then in enhancing $[CHL]_{tot}$ within the LCEs core compared to the background.

IV.4 Eddy-wind interactions

In summer, the total primary production is higher in the background GoM waters as the regenerated production rate is higher. Since grazing is known to be a major contributor of the recycling

loop in the euphotic zone (Sherr and Sherr, 2002), the lower grazing rate inside the LCE during summer (Fig. 9.c.d.) likely explains this lower regenerated production. In addition, the biogeochemical consumption of nitrate that foster the production of organic matter occurs in a deeper layer within the LCEs core compared to the background GoM (Fig. B1. e. f.). It is then more likely exported out of the euphotic layer in the form of settling particle, leading to lower remineralization rates in the upper layers to feed regenerated production. More surprising, the new primary production exhibits similar rates in both regions, although NO_3 depletion occurs deeper in the LCEs core. In the absence of a strong enough vertical mixing when the mixed layer is shallow, this apparent mismatch requires an additional mechanism, vertical advection, capable to supply NO_3 to the euphotic layer (Sweeney et al., 2003; McGillicuddy et al., 2015).

The model vertical velocity in the LCEs reveals an upward pumping in their core (Fig 11). The vertical velocity between 100 and 500 m is on average + 0.07 $m \cdot day^{-1}$. This vertical transport is mainly driven by two mechanisms, eddy pumping (Falkowski et al., 1991) and eddy-wind interaction (Dewar and Flierl, 1987), but their relative importance is difficult to quantify (Gaube et al. 2014; McGillicuddy et al., 2015).

The eddy pumping mechanism is related to the decay of the rotational velocities from the moment LCEs are released from the Loop Current. In the LCE core, this decay is considered as moderate since lateral diffusivity is expected to be relatively low (section V.1). This process may however be considerable in the LCE ring where the erosion rates are important (Meunier at al., 2020).

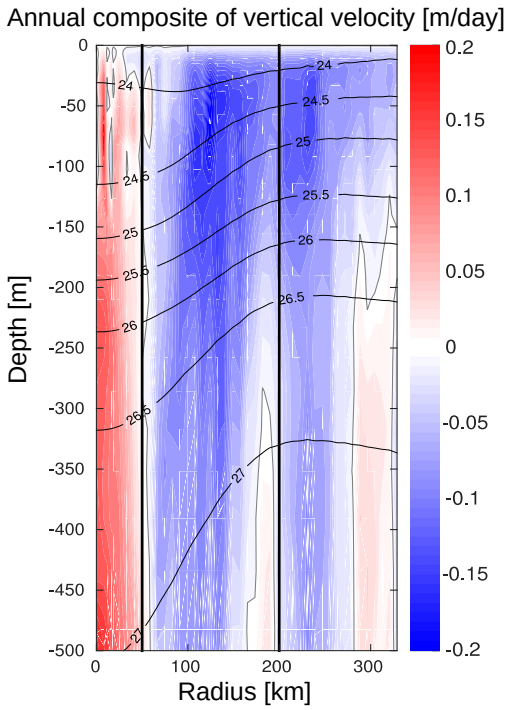

Figure 11: Annually-averaged LCE composite transects of vertical velocities (m/day). Isopycnals anomalies (black contours) are superimposed on all panels. Vertical white lines delimit the three dynamical fields of the LCE composite.

Eddy-wind interactions are due to mesoscale modulation of the Ekman transport, so that they are often qualified as eddy-Ekman pumping (He et al, 2017). Following the observation of a LCE core in quasi-solid body rotation, the horizontal vorticity varies little with the radius resulting in a negligible "non-linear" contribution of the Ekman pumping (McGillicuddy et al., 2008; Gaube et al., 2015). Assuming a small effect of the eddy SST-induced Ekman pumping, the total Ekman pumping simplifies into its "linear" contribution computed as $W_E = \frac{\nabla \times \tau}{\rho_0 . (f + \zeta)}$, where ρ_0 is the surface density, f the Coriolis parameter, τ the stress at the sea surface depending on both the wind and ocean currents at the surface (Martin and Richards, 2001, equation 12) and $\nabla \times$ the curl operator. Considering uniform wind velocities ranging from 4.5 to 7.5 $m \cdot s^{-1}$ (Nowlin & Parker, 1974; Passalacqua et al., 2016) blowing over the LCE, the curl of the stress arises from the anticyclonic surface circulation generated by the eddy. Its manifestation is a persistent horizontal divergence at surface balanced by an upward

pumping in the eddy interior (see Martin & Richards, 2001; Gaube et al., 2013, 2014 for further details). With $\rho_0 \sim 1023$ kg·m^{-3} and $f \sim 6.2.10^{-5}$ s^{-1}, we estimate W_E to range from + 0.06 to 0.13 m·day^{-1}, in agreement with the modeled vertical velocity within the core. The Ekman-eddy pumping mechanism could explain a large fraction of the gradual upwelling within the eddy's core (Fig. 11) and may actively contribute to the advective vertical flux of nutrients (see Appendix B). In summer, this mechanism could explain why new primary production rates are similar in the LCEs core and the background GoM waters although the nutrient pool is located much deeper in the LCEs core.

The eddy-Ekman pumping persists in the LCEs core throughout their lifetime as long as there is a wind stress applied at the surface. During wintertime, we expect that both vertical mixing and eddy-Ekman pumping participate to increase the new primary production. A question then arises on the relative contribution of winter mixing to eddy-Ekman pumping in the LCEs core primary production increase in winter. This issue was tackled by He et al. (2017) and Travis et al. (2019) comparing the rate of change of the mixed layer depth with the vertical velocity induced by the eddy-Ekman pumping (equation 4 in He et al, 2017). In the GoM, even if the wind shows larger magnitudes in winter, it is also associated with a large variability. As a consequence, the variability of Ekman pumping is also found large and a robust seasonal cycle which would allow to isolate the Ekman pumping in winter cannot be clearly identified. However, in the LCEs core, we estimate the mixed layer to deepen at roughly 0.8 m·day^{-1}, which is on average about one order of magnitude larger than the higher bound of the estimated pumping mechanism typically occurring in winter in response to stronger wind events. This supports winter mixing as the overwhelming process for the LCEs-induced primary production peak in winter.

V/ Summary and perspectives

The [CHL] variability induced by the mesoscale Loop Current Eddies in the Gulf of Mexico is studied by analyzing vortex composite fields generated from a coupled physical-biogeochemical model at 1/12° horizontal resolution. LCEs are hotspots for mesoscale biogeochemical variability. Despite the $[CHL]_{surf}$ negative anomaly associated with their core ($r < 50$ km), model results indicate that LCEs are associated with enhanced phytoplankton biomass content, particularly in winter. This enhancement results from the contribution of multiple mechanisms of physical-biogeochemical interactions and contrasts with the background oligotrophic surface waters of the GoM.

The main results of this study are:

- LCEs cores present a negative surface chlorophyll anomaly,
- Unlike $[CHL]_{surf}$, $[CHL]_{tot}$ is larger in the LCEs cores compared to the background GoM in winter.
- LCEs core trigger a large phytoplankton biomass increase in winter,
- The winter mixing is a key mesoscale mechanism that preferentially supplies nutrients to the euphotic layer within the LCEs core. Consequently, it drives an eddy-induced peak of new primary production,
- Ekman-eddy pumping is a significant mechanism for sustaining relatively high new primary production rates within LCE cores during summer.

The phytoplankton biomass increase in individual LCEs cores suggests that LCEs play an important role in sustaining the large-scale GoM productivity.

GOLFO12-PISCES provides numerical results which were largely confronted to observations. This extensive validation gives confidence about its ability to produce realistic seasonal and mesoscale variability of biogeochemical tracers at surface and sub-surface, in particular the one associated with

LCEs. However, biases are inherent to model and might affect the main conclusions drawn. For example, in-situ measurements reveal an intense variability of [CHL] vertical profiles in winter that the model tends to underestimate (Green et al., 2014; Damien et al., 2018). In particular, some individual observed profiles in winter present a DCM while GOLFO12-PISCES largely favors well mixed [CHL] profiles. The under-representation of these profiles, potentially due to a relatively coarse model resolution, could be associated with an under-estimation of $[CHL]_{tot}$ in winter. The results exposed in this study would require further confirmation, notably by more sub-surface in-situ measurements, in particular within the core of LCEs where no [CHL] profiles were observed in winter.

Although the biological response to LCEs may present some specificities due to the particular dynamical nature of LCEs, this study suggests potentially generic insights on the biogeochemical role that anticyclonic eddies could play in oligotrophic environments. It echoes the previous works of Martin and Richards (2001), Gaube et al. (2014, 2015) and especially Dufois et al. (2014, 2016) and He et al. (2017) who proposed winter vertical mixing as an explanation for the positive $[CHL]_{surf}$ anomaly observed in anticyclones in the South Indian Ocean. One of the most crucial points to be underlined from our results is that the enhanced primary production and biomass content within anticyclonic eddies may not necessarily be correlated with the surface layer variability. In oligotrophic areas, the integrated content of chlorophyll in the water column has to be considered. This implies that caution should be exercised in the analysis and interpretation of $[CHL]_{surf}$ observed by remote sensing instruments and highlights the crucial need for in-situ biogeochemical and bio-optical measurements. In oligotrophic environments, defined by their low production rates and their low chlorophyll concentration, anticyclonic eddies are able to trigger local enhanced biological productivity and generate phytoplankton biomass positive anomalies. In a scenario of expansion of oligotrophic areas (Barnett et al., 2001; Behrenfeld et al., 2006; Polovina et al., 2008), the fate and role of mesoscale anticyclones is an important aspect to be considered.

This study focuses on mesoscale physical-biogeochemical interactions which is the spectral range resolved by GOLFO12-PISCES configuration. It evidences the important role of mixing on primary production in the LCE core at seasonal scale. However, mixing also presents significant fluctuations at higher frequencies, associated with particular atmospheric events like storms. The PP_{tot} response to such forcing requires further investigation to verify if the correlation between PP_{tot} and mixing still hold on at higher frequencies where additional other drivers might also become important. For instance, the role of submesoscale is of particular interest since it has been proved to trigger mechanisms of significance importance for biogeochemistry (Levy et al., 2018). Higher model resolutions can locally enhanced density gradients (Levy et al., 2012; Omand et al., 2015) leading to ageostrophic circulations that perturbs the circular flow around vortices (Martin and Richards, 2001) or enhanced vertical velocities that potentially foster the nutrient supply to the euphotic layer. Beside the mesoscale Ekman pumping located at the eddy center, eddy-wind interactions also produce vertical velocities at the eddy periphery (e.g. Flierl and McGillicuddy, 2002). Finally, it is also worth noting that anticyclonic mesoscales eddies are capable of trapping near-inertial energy waves in the ocean (Kunze 1985, Danioux et al. 2008, Koszalka et al. 2010, Pallas-Sanz et al., 2016) where they produce vertical recirculation patterns (Zhong and Bracco, 2013). Even if, some of these dynamical aspects are partially resolved at 1/12° horizontal resolution, higher resolutions simulations with higher frequency outputs are necessary to correctly assess their specific impact.

Acknowledgments: Funding for this study comes from the National Council of Science and Technology of Mexico (CONACYT) -Mexican Ministry of Energy (SENER) Hydrocarbon Trust, project 201441 and a contribution of the Gulf of Mexico Research Consortium (CIGoM), We

589 acknowledge PEMEX’s specific request to the Hydrocarbon Fund to address the environmental effects
590 of oil spills in the Gulf of Mexico. We acknowledge the provision of supercomputing facilities by
591 CICESE.

APPENDIX A: CHL/C-biomass ratio and ecosystem structure

[CHL] is widely used as a proxy for phytosynthetic biomass (Strickland, 1965; Cullen, 1982). However, in addition to depend on phytoplankton concentration, it is also affected by several other factors mainly produced by intracellular physiological mechanisms (Geider, 1987). In particular, photoacclimation processes have been proved to be determinant to explain $[CHL]_{surf}$ variability in oligotrophic areas (Mignot et al. 2014). In the GoM open-waters, this issue was specifically addressed at a basin scale in Pasqueron de Fommervault et al. (2017) considering in-situ particulate backscattering measurements and in Damien et al. (2018) from modeling tools. They both reach the same conclusion: $[CHL]_{tot}$ variability provides a reasonably good estimate of the total C-biomass variability ($[PHY]_{tot}$).

This is confirmed by the small amplitude of the seasonal cycle of the ratio $[CHL]_{tot}/[PHY]_{tot}$ in the background GoM (0.256 +/- 0.004 $g \cdot mol^{-1}$ averaged throughout the year, Fig A1). In the LCEs core, this statement is still valid but must be qualified, since the ratio $[CHL]_{tot}/[PHY]_{tot}$ presents small but significant changes through the year (Fig A1.a). It is around 0.24 $g \cdot mol^{-1}$ from March to November and increases sharply in December to reach about 0.32 $g \cdot mol^{-1}$ in January and February. As a result, in winter, the photoacclimation mechanism accounts for ~25% of the total $[CHL]_{tot}$ increase (the remaining part being an effective phytoplankton biomass increase). In summer, the ratio $[CHL]_{tot}/[PHY]_{tot}$ is slightly lower in the LCEs core compared to the background GoM. As a consequence, the $[CHL]_{tot}$ negative anomaly associated with LCEs core does not necessarily translate into a $[PHY]_{tot}$ negative anomaly.

Overall in the GoM open-waters, there is a dominance of the small-size phytoplankton over the large-size class in proportion closed to 80%:20% (Linacre et al., 2015). Although the modeled

ecosystem structure is relatively simple, this typical community size structure is well reproduced by GOLFO12-PISCES (Fig A1.c and A1.d), that also suggests a shift in the ecosystem structure in winter. The different response among size classes results from the enhancement of nutrient vertical flux. The role of “secondary” nutrient in this change in the community composition must not be overlooked also, in particular for diatoms (accounted in the model’s large-size group) since they also uptake on silicate (Benitez-Nelson et al., 2007). Moreover, GOLFO12-PISCES exhibits a modulation of the ecosystem structure by LCEs. The dominance of small-size phytoplankton is slightly more marked in summer and the winter shift is stronger in the LCEs core.

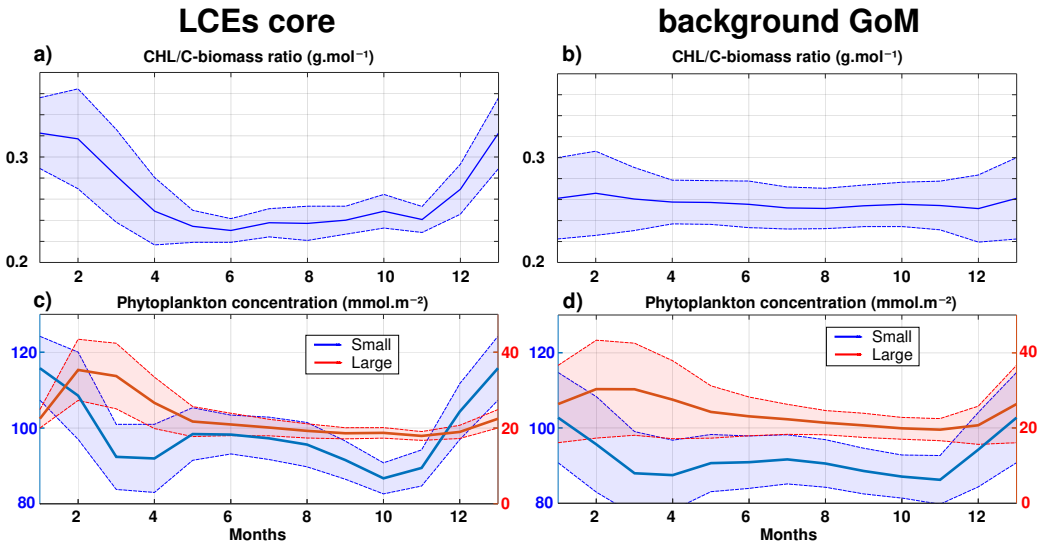

Figure A1: Climatological seasonal cycles of (a and b) the CHL/C-biomass ratio and (c and d) the vertically integrated content of phytoplankton concentration (small size in blue, large size in red). The left panels (a and c) refer to the time series in the LCEs core (r < 50 km) whereas the right panels (b and d) refer to the time series in the background GoM (r > 200 km). For each average cycle, the average value is shown (full line) along with its variability (+/- 1 standard deviation relative to the mean, dashed lines).

APPENDIX B : Nitrate budget at a seasonal scale

Nutrients availability in the euphotic layer is a key mechanism to trigger biomass increase in LCEs. The processes driving the seasonality of nutrient concentrations are here investigated diagnosing the different contributions to nitrate concentrations (hereafter $[NO_3]$) variability. The goal is to confirm the vertical transport of nutrients and quantify the budget in order to determine the driving mechanisms. The analysis is restricted to nitrate concentrations, considered as the main limiting factor for large size-class phytoplankton growth in the GoM (Myers et al., 1981; Turner et al., 2006), although phosphates and silicates are also modeled. We do not exclude that phosphates or silicates could also play a significant role. In cylindrical coordinates, the $[NO_3]$ equation reads:

$$\frac{\partial NO_3}{\partial t} = \underbrace{-V_r \frac{\partial NO_3}{\partial r}}_{\text{radial advection}} \underbrace{- \frac{V_\theta}{r} \frac{\partial NO_3}{\partial \theta}}_{\text{azimuthal advection}} \underbrace{- V_z \frac{\partial NO_3}{\partial z}}_{\text{vertical advection}} \underbrace{+ \frac{D_l}{r} \frac{\partial}{\partial r}\left(r \frac{\partial NO_3}{\partial r} \right) + \frac{D_l}{r^2} \frac{\partial^2 NO_3}{\partial \theta^2}}_{\text{lateral diffusion}} \underbrace{+ \frac{\partial}{\partial z}\left(K_z \frac{\partial NO_3}{\partial z} \right)}_{\text{vertical diffusion}} + \underbrace{SMS}_{\text{Source menus sink}} + Asselin \quad (636)$$

Basically, this is a 3D advection-diffusion equation with added "sources and sinks" terms, namely biogeochemical release and uptake rates. One must include also an "Asselin term", a modeling artifact due to the Asselin time filtering. We focus on the seasonal cycle of three particular trend terms: the vertical mixing (Fig B1.a and B1.b), the vertical advection (Fig B1.c and B1.d) and a "source menus sink" term (Fig B1.e B1.f).

$[NO_3]$ variations from vertical dynamics are mainly positive, especially in the first 100 m of the water column. This traduces in year-round NO_3 source driven by physical processes. By contrast, biogeochemical processes consume NO_3 in the upper layer to sustain the primary production (Fig B1.e and B1.f). In the sub-surface layer (~ below the isoline on which nitrate concentration is equal to 2 $mmol.m^{-3}$), the process of nitrification constitutes a biological source of $[NO_3]$. To first order, this

represents the global functioning of the ecosystem, valid in both fields and throughout the year. However, the seasonal cycle strongly influence the magnitude of these trend terms, in particular in the LCE core.

In winter, from December to February, vertical advective and diffusive motions produce an increase of [NO_3] within the mixed layer. This tendency consists in an advective entrainment resulting from the deepening of the mixed layer which mainly acts to increase [NO_3] at the base of the mixed layer (Fig B1.c and B1.d) and vertical mixing which redistributes vertically the nutrients and tends to homogenize [NO_3] in the mixed layer (Fig B1.a and B1.b). The winter [NO_3] increase is most important in the LCE core at the base of the mixed layer (~ + $6.5.10^{-7}$ mmol·m^{-3}·d^{-1}, nearly 3 times larger than in the background GoM), attesting here a preferential NO_3 uplift due to deeper convection. Integrated over the mixed layer, the winter vertical fluxes produce [NO_3] enhancement of ~ $2.4.10^{-5}$ mmol·m^{-2}·d^{-1} in the eddy core whereas it is only of ~ $1.6.10^{-5}$ mmol·m^{-2}·d^{-1} in the background GoM. This also explains why, on average, the density/nitrate relation differs in the LCEs core (Fig 5.e). In response, the [NO_3] tendency due to biogeochemical processes indicates an increase of the [NO_3] uptake. This increase is about 1.5 times larger in the core (~ - $1.3.10^{-3}$ mmol·m^{-2}·d^{-1} integrated over the mixed layer) than in the background GoM (~ - $0.9.10^{-3}$ mmol·m^{-2}·d^{-1}). Knowing that it feeds biomass production, this [NO_3] loss is consistent with the primary production peak in winter (Fig 9.e and 9.f).

In summer, [NO_3] variations due to vertical processes are smaller than in winter. They are also weaker in the LCEs core upper layer (almost nil in the 0-50m layer) compared to the background GoM, consistent with a deeper NO_3 pool and a shallow mixer layer. In the eddy core, one can assume that the NO_3 vertical supply is entirely consumed before reaching 50m. Below 50m, vertical [NO_3] diffusive trends are consistently more important in the background GoM, in agreement with a steeper nitracline (Fig 5.e). In contrast, vertical [NO_3] advective trends in the eddy core are similar to or can eventually

exceed the trends in the background GoM (as in September and October for example). This confirms a pumping mechanism to sustain primary production in summer within the eddy core (section V.4) The biogeochemical activity related to [NO_3] variations is also less intense in summer compared to winter. The depth of maximum [NO_3] uptake is located just above the DCM and [NO_3] release below. The loss of [NO_3] is about twice larger in the background GoM (~ - $0.9.10^{-7}$ mmol·m^{-3}·d^{-1}) than in the LCEs core (~ - $0.5.10^{-7}$ mmol·m^{-3}·d^{-1}). It is noteworthy that the biogeochemical [NO_3] source term, namely the nitrification rate, is really low within the eddy core.

To close this analysis of the [NO_3] budget, it must be said that lateral diffusion and Asselin tendencies are marginal terms compared to the others. Horizontal advection is of the same order of magnitude as the vertical terms and mainly acts to redistribute horizontally the NO_3 vertically moved (see supplementary material 1).

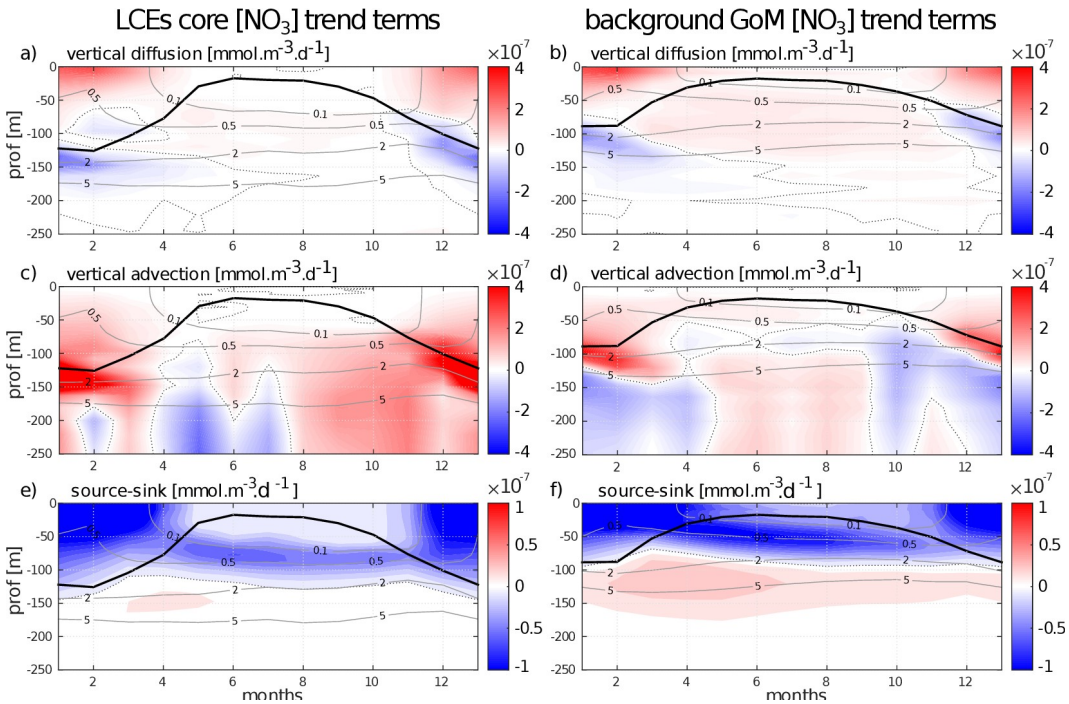

Figure B1: ***Seasonal cycle of nitrate trend terms in the (left column) LCEs core and in the (right column) background GoM. The trend induced by (a and b) vertical mixing, the (c and d) vertical advection and the (e and f) biogeochemical source minus sink are represented. Isopycnals anomalies (gray contours) and the depth of the mixed layer (black line) are superimposed.***

685 **REFERENCES:**

686 Ascani, F., Richards, K. J., Firing, E., Grant, S., Johnson, K. S., Jia, Y., et al. (2013). Physical and
687 biological controls of nitrate concentrations in the upper subtropical North Pacific Ocean. Deep Sea
688 Research, Part II, 93, 119–134.

689 Aumont, O., & Bopp, L. (2006). Globalizing results from ocean in situ iron fertilization studies. Global
690 Biogeochemical Cycles, 20, GB2017. https://doi.org/10.1029/2005GB002591.

691 Aumont, O., Ethé, C., Tagliabue, A., Bopp, L., & Gehlen, M. (2015). PISCES-v2: An ocean
692 biogeochemical model for carbon and ecosystem studies. Geoscientific Model Development, 8(8),
693 2465–2513.

694 Badan Jr, A., Candela, J., Sheinbaum, J., & Ochoa, J. (2005). Upper-layer circulation in the approaches
695 to Yucatan Channel. *Washington DC American Geophysical Union Geophysical Monograph*
696 *Series*, *161*, 57-69.

697 Barnett, T. P., Pierce, D. W., & Schnur, R. (2001). Detection of anthropogenic climate change in the
698 world's oceans. *Science*, *292*(5515), 270-274.

699 Behrenfeld, M. J., O'Malley, R. T., Siegel, D. A., McClain, C. R., Sarmiento, J. L., Feldman, G. C., ...
700 & Boss, E. S. (2006). Climate-driven trends in contemporary ocean productivity. *Nature*, *444*(7120),
701 752.

Benitez-Nelson, C. R., Bidigare, R. R., Dickey, T. D., Landry, M. R., Leonard, C. L., Brown, S. L., ... & Bibby, T. S. (2007). Mesoscale eddies drive increased silica export in the subtropical Pacific Ocean. *Science*, *316*(5827), 1017-1021.

Biggs, D. C., & Ressler, P. H. (2001). Distribution and abundance of phytoplankton, zooplankton, ichthyoplankton, and micronekton in the deepwater Gulf of Mexico. *Gulf of Mexico Science*, *19*(1), 2.

Bracco, A., Provenzale, A., & Scheuring, I. (2000). Mesoscale vortices and the paradox of the plankton. *Proceedings of the Royal Society of London B: Biological Sciences*, *267*(1454), 1795-1800.

Brodeau, L., Barnier, B., Treguier, A.-M., Penduff, T., & Gulev, S. (2010). An ERA40-based atmospheric forcing for global ocean circulation models. Ocean Modelling, 31, 88–104. https://doi.org/10.1016/j.ocemod.2009.10.005

Brokaw, R. J., Subrahmanyam, B., & Morey, S. L. (2019), Loop current and eddy driven salinity variability in the Gulf of Mexico, *Geophysical Research Letters*, *46*, 5978–5986, https://doi.org/10.1029/2019GL082931.

Chelton, D., DeSzoeke, R., Schlax, M., El Naggar, K., & Siwertz, N. (1998). Geographical variability of the first baroclinic Rossby radius of deformation. Journal of Physical Oceanography, 28(3), 433–460.

Ciani, D., Carton, X., Aguiar, A. B., Peliz, A., Bashmachnikov, I., Ienna, F., ... & Santoleri, R. (2017). Surface signature of Mediterranean water eddies in a long-term high-resolution simulation. *Deep Sea Research Part I: Oceanographic Research Papers*, *130*, 12-29.

721 Cooper, C., Forristall, G. Z., & Joyce, T. M. (1990). Velocity and hydrographic structure of two Gulf of
722 Mexico warm-core rings. *Journal of Geophysical Research: Oceans*, *95*(C2), 1663-1679.

723 Cullen, J. J. (1982). The deep chlorophyll maximum: Comparing vertical profiles of chlorophyll a.
724 Canadian Journal of Fisheries and Aquatic Sciences, 39(5), 791–803.

725 Dai, A., & Trenberth, K. E. (2002). Estimates of freshwater discharge from continents: Latitudinal and
726 seasonal variations. Journal of Hydro-meteorology, 3, 660–687.

727 Damien, P., Pasqueron de Fommervault, O., Sheinbaum, J., Jouanno, J., Camacho-Ibar, V. F., &
728 Duteil, O. (2018). Partitioning of the Open Waters of the Gulf of Mexico Based on the Seasonal and
729 Interannual Variability of Chlorophyll Concentration. *Journal of Geophysical Research: Oceans*.

730 Danioux, E., Klein, P., & Rivière, P. (2008). Propagation of wind energy into the deep ocean through a
731 fully turbulent mesoscale eddy field. *Journal of Physical Oceanography*, *38*(10), 2224-2241.

732 Dewar, W., and G. Flierl (1987), Some effects of the wind on rings, J. Phys. Oceanogr., 17(10), 1653–
733 1667.

734 Doney, S. C., Glover, D. M., McCue, S. J., & Fuentes, M. (2003). Mesoscale variability of Sea-viewing
735 Wide Field-of-view Sensor (SeaWiFS) satellite ocean color: Global patterns and spatial scales. *Journal*
736 *of Geophysical Research: Oceans*, *108*(C2).

737 Dong, C., X. Lin, Y. Liu, F. Nencioli, Y. Chao, Y. Guan, D. Chen, T. Dickey, and J. C. McWilliams
738 (2012), Three-dimensional oceanic eddy analysis in the Southern California Bight from a numerical
739 product, J. Geophys. Res., 117, C00H14, doi:10.1029/2011JC007354.

740 Donohue, Kathleen A., et al. "Loop current eddy formation and baroclinic instability." *Dynamics of*
741 *Atmospheres and Oceans* 76 (2016): 195-216.

742 d'Ovidio, F., De Monte, S., Della Penna, A., Cotté, C., & Guinet, C. (2013). Ecological implications of
743 eddy retention in the open ocean: a Lagrangian approach. *Journal of Physics A: Mathematical and*
744 *Theoretical*, *46*(25), 254023.

745 Dufois, F., Hardman-Mountford, N. J., Greenwood, J., Richardson, A. J., Feng, M., Herbette, S., &
746 Matear, R. (2014). Impact of eddies on surface chlorophyll in the South Indian Ocean. *Journal of*
747 *Geophysical Research: Oceans*, *119*(11), 8061-8077.

748 Dufois, F., Hardman-Mountford, N. J., Greenwood, J., Richardson, A. J., Feng, M., & Matear, R. J.
749 (2016). Anticyclonic eddies are more productive than cyclonic eddies in subtropical gyres because of
750 winter mixing. *Science advances*, *2*(5), e1600282.

751 Dufois, F., Hardman-Mountford, N. J., Fernandes, M., Wojtasiewicz, B., Shenoy, D., Slawinski, D., ...
752 & Toresen, R. (2017). Observational insights into chlorophyll distributions of subtropical South Indian
753 Ocean eddies. *Geophysical Research Letters*, *44*(7), 3255-3264.

754 Dugdale, R. C., and J. J. Goering (1967), Uptake of new and regenerated forms of nitrogen in primary
755 productivity, Limnol. Oceanogr., 12, 196–206

Early, J. J., Samelson, R. M., & Chelton, D. B. (2011). The evolution and propagation of quasigeostrophic ocean eddies. *Journal of Physical Oceanography*, *41*(8), 1535-1555.

Elliott, B. A. (1982). Anticyclonic rings in the Gulf of Mexico. *Journal of Physical Oceanography*, *12*(11), 1292-1309.

Eppley, R. W., and B. J. Peterson (1979), Particulate organic matter flux and planktonic new production in the deep ocean, Nature, 282, 677–680.

Falkowski, P., D. Ziemann, Z. Kolber, and P. Bienfang (1991), Role of eddy pumping in enhancing primary production in the ocean, Nature, 352(6330), 55–58.

Flierl, G. R. (1981). Particle motions in large-amplitude wave fields. *Geophysical & Astrophysical Fluid Dynamics*, *18*(1-2), 39-74.

Flierl, G. R., & McGillicuddy, D. J. (2002). Mesoscale and submesoscale physical-biological interactions. *The sea*, *12*, 113-185.

de Fommervault, O. P., Perez-Brunius, P., Damien, P., Camacho-Ibar, V. F., & Sheinbaum, J. (2017). Temporal variability of chlorophyll distribution in the Gulf of Mexico: bio-optical data from profiling floats. *Biogeosciences*, *14*(24), 5647.

771 Forristall, G. Z., Schaudt, K. J., & Cooper, C. K. (1992). Evolution and kinematics of a Loop Current
772 eddy in the Gulf of Mexico during 1985. *Journal of Geophysical Research: Oceans*, *97*(C2), 2173-
773 2184.

774 Frolov, S. A., et al. "Loop Current eddy interaction with the western boundary in the Gulf of Mexico."
775 *Journal of physical oceanography* 34.10 (2004): 2223-2237.

776 Garcia, H. E., Locarnini, R. A., Boyer, T. P., Antonov, J. I., Baranova, O. K., Zweng, M. M., et al.
777 (2010). World Ocean Atlas 2009. In S. Levitus (Ed.), Dissolved oxygen, apparent oxygen utilization,
778 and oxygen saturation (NOAA Atlas NESDIS 70, Vol. 3, 344 p.). Washington, DC: U.S. Government.
779 Printing Office.

780 Garcia-Jove Navarro, M., Sheinbaum Pardo, J., & Jouanno, J. (2016). Sensitivity of Loop Current
781 metrics and eddy detachments to different model configurations: The impact of topography and
782 Caribbean perturbations. Atmosfera, 29(3), 235–265. https://doi.org/10.20937/ATM.2016.29.03.05

783 Garçon, V. C., Oschlies, A., Doney, S. C., McGillicuddy, D., & Waniek, J. (2001). The role of
784 mesoscale variability on plankton dynamics in the North Atlantic. *Deep Sea Research Part II: Topical*
785 *Studies in Oceanography*, *48*(10), 2199-2226.

786 Gaube, P., Chelton, D. B., Strutton, P. G., & Behrenfeld, M. J. (2013). Satellite observations of
787 chlorophyll, phytoplankton biomass, and Ekman pumping in nonlinear mesoscale eddies. *Journal of*
788 *Geophysical Research: Oceans*, *118*(12), 6349-6370.

Gaube, P., McGillicuddy, D. J., Chelton, D. B., Behrenfeld, M. J., & Strutton, P. G. (2014). Regional variations in the influence of mesoscale eddies on near-surface chlorophyll. *Journal of Geophysical Research: Oceans*, *119*(12), 8195-8220.

Gaube, P., Chelton, D. B., Samelson, R. M., Schlax, M. G., & O'Neill, L. W. (2015). Satellite observations of mesoscale eddy-induced Ekman pumping. *Journal of Physical Oceanography*, *45*(1), 104-132.

Geider, R. J. (1987), Light and temperature dependence of the carbon to chlorophyll a ratio in microalgae and cyanobacteria: implications for physiology and growth of phytoplankton, New Phytol., 106, 1–34.

Geider, R. J., MacIntyre, H. L., & Kana, T. M. (1997). A dynamical model of phytoplankton growth and acclimation: Response of the balanced growth rate to light, nutrient limitation and temperature. Marine Ecology Progress Series, 148, 187–200.

Glenn, S. M., and C. C. Ebbesmeyer (1993), Drifting buoy observations of a loop current anticyclonic eddy, J. Geophys. Res., , 98, 20, doi:10.1029/93JC02078.

Green, R. E., Bower, A. S., & Lugo-Fernández, A. (2014). First autonomous bio-optical profiling float in the Gulf of Mexico reveals dynamic biogeochemistry in deep waters. *PloS one*, *9*(7), e101658.

Guo, M., P. Xiu, S. Li, F. Chai, H. Xue, K. Zhou, and M. Dai (2017), Seasonal variability and mechanisms regulating chlorophyll distribution in mesoscale eddies in the South China Sea, J. Geophys. Res. Oceans, 122, 5329–5347, doi:10.1002/2016JC012670.

Hamilton, P., Leben, R., Bower, A., Furey, H., & Pérez-Brunius, P. (2018). Hydrography of the Gulf of Mexico Using Autonomous Floats. *Journal of Physical Oceanography*, *48*(4), 773-794. DOI: 10.1175/JPO-D-17-0205.1

Hamilton, P. (2007). Eddy statistics from Lagrangian drifters and hydrography for the northern Gulf of Mexico slope. Journal of Geophysical Research, 112, C09002. https://doi.org/10.1029/2006JC003988

He, Q., Zhan, H., Shuai, Y., Cai, S., Li, Q. P., Huang, G., & Li, J. (2017). Phytoplankton bloom triggered by an anticyclonic eddy: The combined effect of eddy Ekman pumping and winter mixing. *Journal of Geophysical Research: Oceans*, *122*(6), 4886-4901.

Hernandez-Guerra, A., & Joyce, T. M. (2000). Water masses and circulation in the surface layers of the Caribbean at 66 W. Geophysical Research Letters, 27(21), 3497–3500. https://doi.org/10.1029/1999GL011230

Herrmann, M., Somot, S., Sevault, F., Estournel, C., & Deque, M. (2008). Modeling the deep convection in the northwestern Mediterranean Sea using an eddy-permitting and an eddy-resolving model: Case study of winter 1986–1987. Journal of Geophysical Research, 113, C04011. https://doi.org/10.1029/2006JC003991

Huang, J., & Xu, F. (2018). Observational evidence of subsurface chlorophyll response to mesoscale eddies in the North Pacific. Geophysical Research Letters, 45, 8462–8470. https://doi.org/10.1029/2018GL078408

826 Jolliff, J. K., Kindle, J. C., Penta, B., Helber, R., Lee, Z., Shulman, I., Arnone, R., and Rowley, C. D.,
827 (2008). On the relationship between satellite-estimated bio-optical and thermal properties in the Gulf of
828 Mexico, J. Geophys. Res., 113, G1, https://doi.org/10.1029/2006JG000373

829 Jouanno, J., Ochoa de la Torre, J. L., Pallas Sanz, E., Sheinbaum Pardo, J., Andrade Canto, F., Candela
830 Perez, J., et al. (2016). Loop current frontal eddies: Formation along the Campeche Bank and impact of
831 coastally trapped waves. Journal of Physical Oceanography, 46(11), 3339–3363.
832 https://doi.org/10.1175/JPO-D-16-0052.1

833 Klein, P., & Lapeyre, G. (2009). The oceanic vertical pump induced by mesoscale and submesoscale
834 turbulence. *Annual review of marine science*, *1*, 351-375.

835 Koszalka, I. M., Ceballos, L., & Bracco, A. (2010). Vertical mixing and coherent anticyclones in the
836 ocean: the role of stratification. *Nonlinear Processes in Geophysics*, *17*(1), 37-47.

837 Kouketsu, S., Tomita, H., Oka, E., Hosoda, S., Kobayashi, T., & Sato, K. (2011). The role of meso-
838 scale eddies in mixed layer deepening and mode water formation in the western North Pacific. In *New*
839 *Developments in Mode-Water Research* (pp. 59-73). Springer, Tokyo.

840 Kunze, E. (1985). Near-inertial wave propagation in geostrophic shear. *Journal of Physical*
841 *Oceanography*, *15*(5), 544-565.

842 Lascaratos, A., & Nittis, K. (1998). A high-resolution three-dimensional numerical study of
843 intermediate water formation in the Levantine Sea. Journal of Geophysical Research, 103(C9), 18497–
844 18511.

845 Lehahn, Y., F. d'Ovidio, M. Levy, Y. Amitai, and E. Heifetz (2011), Long range transport of a quasi
846 isolated chlorophyll patch by an Agulhas ring, Geophys. Res. Lett., 38, L16610,
847 doi:10.1029/2011GL048588.

848 Le Hénaff, M., Kourafalou, V. H., Morel, Y., & Srinivasan, A. (2012). Simulating the dynamics and
849 intensification of cyclonic Loop Current Frontal Eddies in the Gulf of Mexico. *Journal of Geophysical*
850 *Research: Oceans*, *117*(C2).

851 Levitus, S. (1982). Climatological atlas of the world ocean (NOAA Prof. Pap. 13, 173 p.). Washington,
852 DC: U.S. Government Printing Office.

853 Lévy, M., Ferrari, R., Franks, P. J., Martin, A. P., & Rivière, P. (2012). Bringing physics to life at the
854 submesoscale. *Geophysical Research Letters*, *39*(14).

855 Lévy, M., Franks, P.J.S. & Smith, K.S. (2018). The role of submesoscale currents in structuring marine
856 ecosystems. *Nat. Commun.*, **9,** 4758

857 Linacre, L., Lara-Lara, R., Camacho-Ibar, V., Herguera, J. C., Bazán-Guzmán, C., & Ferreira-Bartrina,
858 V. (2015). Distribution pattern of picoplankton carbon biomass linked to mesoscale dynamics in the
859 southern gulf of Mexico during winter conditions. *Deep Sea Research Part I: Oceanographic Research*
860 *Papers*, *106*, 55-67.

861 Linacre, L., Durazo, R., Camacho-Ibar, V. F., Selph, K. E., Lara-Lara, J. R., Mirabal-Gómez, U., ... &
862 Sidón-Ceseña, K. (2019). Picoplankton Carbon Biomass Assessments and Distribution of

Prochlorococcus Ecotypes Linked to Loop Current Eddies During Summer in the Southern Gulf of Mexico. *Journal of Geophysical Research: Oceans*, *124*(11), 8342-8359.

Lipphardt, B., Poje, A. C., Kirwan, A., Kantha, L., & Zweng, M. (2008). Death of three Loop Current rings. *Journal of Marine Research*, *66*(1), 25-60.

Madec, G. (2016). NEMO ocean engine, Note Du Pole De Mod# elisation (Vol. 27, 406 p.). Paris, France: Institut Pierre-Simon Laplace.

Mann, K. H., & Lazier, J. R. N. (2006). Dynamics of marine ecosystems (3rd ed.). Oxford, UK: Blackwell Publishing.

Mahadevan, A. (2014). Ocean science: Eddy effects on biogeochemistry. *Nature*, *506*(7487), 168.

Martin, A. P., & Richards, K. J. (2001). Mechanisms for vertical nutrient transport within a North Atlantic mesoscale eddy. *Deep Sea Research Part II: Topical Studies in Oceanography*, *48*(4-5), 757-773.

Mayot, N., D'Ortenzio, F., Taillandier, V., Prieur, L., de Fommervault, O. P., Claustre, H., ... & Conan, P. (2017). Physical and biogeochemical controls of the phytoplankton blooms in North Western Mediterranean Sea: A multiplatform approach over a complete annual cycle (2012–2013 DEWEX experiment). *Journal of Geophysical Research: Oceans*, *122*(12), 9999-10019.

McClain, C. R., Signorini, S. R., & Christian, J. R. (2004). Subtropical gyre variability observed by ocean-color satellites. *Deep Sea Research Part II: Topical Studies in Oceanography*, *51*(1-3), 281-301.

McGillicuddy, D. J., Jr. (2016), Mechanisms of Physical-Biological-Biogeochemical Interaction at the Oceanic Mesoscale, Annu. Rev. Mar. Sci., 8, 125–159, doi:10.1146/annurev-marine-010814-015606.

McGillicuddy Jr, D. J., Robinson, A. R., Siegel, D. A., Jannasch, H. W., Johnson, R., Dickey, T. D., ... & Knap, A. H. (1998). Influence of mesoscale eddies on new production in the Sargasso Sea. *Nature*, *394*(6690), 263.

McGillicuddy Jr, D. J., & Robinson, A. R. (1997). Eddy-induced nutrient supply and new production in the Sargasso Sea. *Deep Sea Research Part I: Oceanographic Research Papers*, *44*(8), 1427-1450.

Meunier, T., Sheinbaum, J., Pallàs-Sanz, E., Tenreiro, M., Ochoa, J., Ruiz-Angulo, A., ... & de Marez, C. (2020). Heat Content Anomaly and Decay of Warm-Core Rings: the Case of the Gulf of Mexico. *Geophysical Research Letters*, *47*(3), e2019GL085600.

Meunier, T., Tenreiro, M., Pallàs-Sanz, E., Ochoa, J., Ruiz-Angulo, A., Portela, E., et al. (2018a). Intrathermocline eddies embedded within an anticyclonic vortex ring. Geophysical Research Letters, 45. https://doi.org/10.1029/2018GL077527

Meunier, T., Pallás-Sanz, E., Tenreiro, M., Rodriguez, E. P., Ochoa, J., Ruiz-Angulo, A., & Cusí, S. (2018b). The Vertical structure of a Loop Current Eddy. *Journal of Geophysical Research: Oceans*.

Mignot, A., Claustre, H., Uitz, J., Poteau, A., D'Ortenzio, F., and Xing, X., (2014), Understanding the seasonal dynamics of phytoplankton biomass and the deep chlorophyll maximum in oligotrophic environments: A Bio-Argo float investigation, Global Biogeochem. Cy., 28, 856–876.

Monterey, G., & Levitus, S. (1997). Seasonal variability of mixed layer depth for the World Ocean (NOAA Atlas NESDIS 14, 100 p.). Silver Spring, MD: National Oceanic and Atmospheric Administration.

Muller-Karger, F. E., Walsh, J. J., Evans, R. H., & Meyers, M. B. (1991). On the seasonal phytoplankton concentration and sea surface temperature cycles of the Gulf of Mexico as determined by satellites. Journal of Geophysical Research, 96(C7), 12645–12665.

Myers, V. B., & Iverson, R. I. (1981). Phosphorus and nitrogen limited phytoplankton productivity in northeastern Gulf of Mexico coastal estuaries. In *Estuaries and nutrients* (pp. 569-582). Humana Press.

Nencioli, F., C. Dong, T. Dickey, L. Washburn, and J. C. McWilliams (2010), A vector geometry-based eddy detection algorithm and its application to a high-resolution numerical model product and high-frequency radar surface velocities in the Southern California Bight, J. Atmos. Oceanic Technol., 27, 564–579, doi:10.1175/2009JTECHO725.1.

Nof, D., 1981: On the b-induced movement of isolated baroclinic eddies. J. Phys. Oceanogr., 11, 1662–1672, https://doi.org/ 10.1175/1520-0485(1981)011,1662:OTIMOI.2.0.CO;2.

Nowlin, W. D. Jr., & Parker, C. A. (1974). Effects of a cold-air outbreak on shelf waters of the Gulf of Mexico. Journal of Physical Oceanography, 4(3), 467–486.

915 Omand, M. M., D'Asaro, E. A., Lee, C. M., Perry, M. J., Briggs, N., Cetinić, I., & Mahadevan, A.
916 (2015). Eddy-driven subduction exports particulate organic carbon from the spring bloom. *Science*,
917 *348*(6231), 222-225.

918 Omand, M. M., & Mahadevan, A. (2014). Shape of the oceanic nitracline. Biogeosciences Discussions,
919 11, 14729–14763.

920 Oschlies, A., & Garcon, V. (1998). Eddy-induced enhancement of primary production in a model of the
921 North Atlantic Ocean. *Nature*, *394*(6690), 266.

922 Pallàs-Sanz, E., Candela, J., Sheinbaum, J., Ochoa, J., & Jouanno, J. (2016). Trapping of the near-
923 inertial wave wakes of two consecutive hurricanes in the Loop Current. *Journal of Geophysical*
924 *Research: Oceans*, *121*(10), 7431-7454.

925 Passalacqua, G. A., Sheinbaum, J., & Martinez, J. A. (2016). Sea surface temperature influence on a
926 winter cold front position and propagation: Air-sea interactions of the 'Nortes' winds in the Gulf of
927 Mexico. Atmospheric Science Letters, 17(5), 302–307.

928 Polovina, J. J., Howell, E. A., & Abecassis, M. (2008). Ocean's least productive waters are expanding.
929 *Geophysical Research Letters*, *35*(3).

930 Sathyendranath, S, Brewin, RJW, Müeller, D, Brockmann, C, Deschamps, P-Y, Doerffer, R, Fomferra,
931 N, Franz, BA, Grant, MG, Hu C, Krasemann, H, Lee, Z, Maritorena, S, Devred, E, Mélin, F, Peters, M,
932 Smyth, T, Steinmetz, F, Swinton, J, Werdell, J, Regner, P (2012) Ocean Colour Climate Change

933 Initiative: Approach and Initial Results, IGARSS 2012, 2024-2027.
934 doi:10.1109/IGARSS.2012.6350979.

935 Sheinbaum Pardo, J., Athie De Velasco, G. E., Candela Perez, J., Ochoa de la Torre, J. L., & Romero
936 Arteaga, A. M. (2016). Structure and variability of the Yucatan and loop currents along the slope and
937 shelf break of the Yucatan channel and Campeche bank. Dynamics of Atmospheres and Oceans, 76,
938 217–239. https://doi.org/10.1016/j.dynatmoce.2016.08.001

939 Sherr, E. B., & Sherr, B. F. (2002). Significance of predation by protists in aquatic microbial food
940 webs. *Antonie van Leeuwenhoek*, *81*(1), 293-308.

941 Siegel, D. A., Behrenfeld, M. J., Maritorena, S., McClain, C. R., Antoine, D., Bailey, S. W., ... & Eplee
942 Jr, R. E. (2013). Regional to global assessments of phytoplankton dynamics from the SeaWiFS
943 mission. *Remote Sensing of Environment*, *135*, 77-91.

944 Siegel, D. A., McGillicuddy Jr, D. J., & Fields, E. A. (1999). Mesoscale eddies, satellite altimetry, and
945 new production in the Sargasso Sea. *Journal of Geophysical Research: Oceans*, *104*(C6), 13359-
946 13379.

947 Sosa-Gutiérrez, R., et al. "Erosion of the Subsurface Salinity Maximum of the Loop Current Eddies
948 From Glider Observations and a Numerical Model." *Journal of Geophysical Research: Oceans* 125.7
949 (2020): e2019JC015397.

950 Strickland, J. D. H. (1965). Production of organic matter in the primary stages of the marine food
951 chain, Chem. Oceanogr., 1, 477–610.

952 Sturges, W., & Leben, R. (2000). Frequency of ring separations from the Loop Current in the Gulf of
953 Mexico: A revised estimate. Journal of Physical Oceanography, 30, 1814–1819.

954 Sturges, W., & Kenyon, K. E. (2008). Mean flow in the Gulf of Mexico. *Journal of Physical*
955 *Oceanography*, *38*(7), 1501-1514.

956 Sweeney, E. N., D. J. McGillicuddy, and K. O. Buesseler (2003), Biogeochemical impacts due to
957 mesoscale eddy activity in the Sargasso Sea as measured at the Bermuda Atlantic Time-series Study
958 (BATS), Deep Sea Res., Part II, 50(22–26), 3017–3039, doi:10.1016/j.dsr2.2003.07.008.

959 Tenreiro, M., Candela, J., Sanz, E. P., Sheinbaum, J., & Ochoa, J. (2018). Near-Surface and Deep
960 Circulation Coupling in the Western Gulf of Mexico. *Journal of Physical Oceanography*, *48*(1), 145-
961 161.

962 Travis, S., & Qiu, B. (2020). Seasonal Reversal of the Near-Surface Chlorophyll Response to the
963 Presence of Mesoscale Eddies in the South Pacific Subtropical Countercurrent. *Journal of Geophysical*
964 *Research: Oceans*, *125*(3), e2019JC015752.

965 Turner, J. S. (1973). Buoyancy effects in fluids (368 p.). New York, NY: Cambridge University Press.

966 Turner, R. E., Rabalais, N. N., & Justic, D. (2006). Predicting summer hypoxia in the northern Gulf of
967 Mexico: Riverine N, P, and Si loading. *Marine pollution bulletin*, *52*(2), 139-148.

968 Vukovich, F. M., 2007: Climatology of ocean features in the Gulf of Mexico using satellite remote
969 sensing data. J. Phys. Oceanogr., 37, 689–707, https://doi.org/10.1175/JPO2989.1.

970 Waite, A. M., S. Pesant, D. A. Griffin, P. A. Thompson, and C. M. Holl (2007), Oceanography,
971 primary production and dissolved inorganic nitrogen uptake in two Leeuwin Current eddies, Deep Sea
972 Res., Part II, 54(8–10), 981–1002, doi:10.1016/j.dsr2.2007.03.001.

973 Wawrik,B.,Paul,J.,Bronk,D.,John,D.,Gray,M.,2004.High rates of ammonium recycling drive
974 phytoplankton productivity in the offshore Mississippi River plume. Aquat.Microb.Ecol.35,175–184.
975 http://dx.doi.org/10.3354/ame035175.

976 Weisberg, R. H., & Liu, Y. (2017). On the Loop Current penetration into the Gulf of Mexico. *Journal*
977 *of Geophysical Research: Oceans*, *122*(12), 9679-9694.

978 Williams, R. G. (1988). Modification of ocean eddies by air-sea interaction. *Journal of Geophysical*
979 *Research: Oceans*, *93*(C12), 15523-15533.

980 WuuSt, G. (1964). Stratification and circulation in the Antillean-Caribbean basins (Vol. 1). New York,
981 NY: Columbia University Press.

982 Zhao, J., Bower, A., Yang, J., & Lin, X. (2018). Meridional heat transport variability induced by
983 mesoscale processes in the subpolar North Atlantic. *Nature communications*, *9*(1), 1124.

984 Zhong, Y., & Bracco, A. (2013). Submesoscale impacts on horizontal and vertical transport in the Gulf
985 of Mexico, *Journal of Geophysical Research: Oceans, 118(10)*, 5651-5668.